Regulator artifacts in uniform matter for chiral interactions

A. Dyhdalo, R. J. Furnstahl, K. Hebeler, and I. Tews

Phys. Rev. C **94**, 034001 — Published 2 September 2016

DOI: 10.1103/PhysRevC.94.034001

Regulator Artifacts in Uniform Matter for Chiral Interactions

A. Dyhdalo,[1,*] R.J. Furnstahl,[1,†] K. Hebeler,[2,3,‡] and I. Tews[2,3,4,§]

[1] *Department of Physics, The Ohio State University, Columbus, OH 43210, USA*
[2] *Institut für Kernphysik, Technische Universität Darmstadt, 64289 Darmstadt, Germany*
[3] *ExtreMe Matter Institute EMMI, GSI Helmholtzzentrum für Schwerionenforschung GmbH, 64291 Darmstadt, Germany*
[4] *Institute for Nuclear Theory, University of Washington, Seattle, WA 98195-1550*

(Dated: August 7, 2016)

Regulator functions applied to two- and three-nucleon forces are a necessary ingredient in many-body calculations based on chiral effective field theory interactions. These interactions have been developed recently with a variety of different cutoff forms, including regulating both the momentum transfer (local) and the relative momentum (nonlocal). While in principle any regulator that suppresses high momentum modes can be employed, in practice artifacts are inevitable in current power counting schemes. Artifacts from particular regulators may cause significant distortions of the physics or may affect many-body convergence rates, so understanding their nature is important. Here we characterize the differences between cutoff effects using uniform matter at Hartree-Fock and second-order in the interaction as a testbed. This provides a clean laboratory to isolate phase-space effects of various regulators on both two- and three-nucleon interactions. We test the normal-ordering approximation for three-nucleon forces in nuclear matter and find that the relative size of the residual 3N contributions is sensitive to the employed regularization scheme.

I. INTRODUCTION

Chiral Effective Field Theory (χEFT) [1, 2] has become the method of choice for input Hamiltonians and other operators needed for *ab initio* calculations of few- and many-body nuclear systems [3–24]. χEFT respects the low-energy symmetries of QCD and promises to be model-independent, systematically improvable in an order-by-order expansion, and have controlled uncertainties from omitted terms. χEFT is not uniquely specified and there are different competing implementations. Hereafter, when we use the term χEFT, we are referring specifically to the Weinberg power counting scheme with no explicit Δ-isobar [1, 2].

As with any quantum field theory, the presence of loops requires the introduction of a regularization scheme and scale. Nonperturbativeness of the nucleon-nucleon (NN) system, as manifested by the shallow deuteron bound state and large singlet S-wave scattering length, implies the need to resum certain classes of diagrams. For the power counting prescription introduced by Weinberg [25, 26], the NN potential is truncated at a specified order in the chiral expansion and then iterated, e.g., in the Lippmann-Schwinger equation. An analogous procedure is used for many-body forces, e.g., three-nucleon (3N) forces, which are constructed in the chiral expansion and iterated, e.g., in the Faddeev equations [27]. Ultraviolet (UV) divergences arise both in the construction of the nuclear potential and in its iteration. For the latter, cutoff regularization is applied in all current applications of χEFT.

In implementing the cutoff regularization we specify a function, called a regulator, that suppresses the nuclear potentials above a regularization scale Λ, called the cutoff. The regulator is treated as an *intrinsic* part of the potential and not a separate entity associated only with divergent loops. Regulators by construction separate unresolved UV physics from explicit infrared (IR) physics, whereupon the UV physics is implicitly incorporated via the Lagrangian low-energy constants (LECs). We require that the regulator be sufficiently smooth (i.e., not a step function), so that it can be used in basis transformations, but this leaves much freedom in the functional form.

The inclusion of long-range pions in the iteration for Weinberg power counting means that χEFT is not fully renormalized order by order [28]. That is, there remains a residual cutoff dependence in the theory at each order. The residual scale and scheme dependences are what we call "regulator artifacts" (note that regulator artifacts also include regularization dependencies due to breaking symmetries e.g., Lorentz invariance). To achieve full model-independence in an EFT, the *predictions* of the theory must demonstrate an insensitivity to the choice of regulator and cutoff scale. But in contrast to other field theories (e.g., QED), the individual contributions in chiral EFT do not vary logarithmically but much more rapidly with the cutoff. Thus, special attention must be paid to the scheme and scale being adopted. The present work seeks to make the impact of these choices and associated regulator artifacts more transparent (see Ref. [29] for a discussion of regulator dependence for lattice EFT).

As many-body methods have become increasingly accurate, the focus has shifted back to the chiral Hamiltonian. Better understanding of renormalization in Weinberg power counting and being able to quantify uncertainties will be crucial to future precision tests of χEFT. Below, we highlight various issues involving regulators arising in current applications.

* dyhdalo.2@osu.edu
† furnstahl.1@osu.edu
‡ kai.hebeler@physik.tu-darmstadt.de
§ itews@uw.edu

- There needs to be adequate suppression of the short-range parts of the long-range (pion) potentials. Regularization of the singular structure in pion exchanges demonstrates some of these subtleties [30–32], e.g., spurious bound states if the cutoff is chosen too high. The functional form of the regulator is also found to impact artifacts in the form of residual cutoff dependence [33].

- In addition to cutting off UV physics, regulators should avoid distorting the long-range (IR) parts of the nuclear potentials [33] as these parts of the force are assumed to be rigorously connected to QCD through chiral symmetry.

- Some many-body methods, such as Auxiliary Field Diffusion Monte Carlo (AFDMC) and Green's Function Monte Carlo (GFMC), need local potentials and local regulators to avoid large statistical uncertainties [34–36].

- Regulators can impact the convergence of many-body methods at finite density. A common many-body approximation used with 3N forces is to normal-order them with respect to a finite density reference state [37]. This leads to density-dependent 0-, 1-, and 2-body terms plus a residual 3-body part. The residual contribution is usually assumed to be small (in some cases there has been a numerical check) and discarded for computational efficiency (e.g., see Ref. [4]).

The regulator choice has effects on each of these issues.

To assess the regulator dependence in χEFT, we propose studying these interactions *perturbatively* in a uniform system. Applying many-body perturbation theory (MBPT) is particularly clean and simple in this case, and allows the effects of the regulator to be isolated without worrying about complications such as finite size effects. We confine ourselves to the regulator's impact on the Hartree-Fock (HF) and second-order energy to demonstrate effects for the IR and UV parts of the interaction. We also restrict our attention in this paper to the LO NN and N^{2}LO 3N interaction terms derived in χEFT at, respectively, order $\nu = 0$ and $\nu = 2$ in the chiral expansion. These are sufficiently rich for the present investigation. We assume natural sizes for all LEC coefficients and do not fit the forces to experimental data (e.g., phase shifts).

With one exception at 3N second-order, we work with pure neutron matter (PNM), which is more perturbative and simpler to analyze than symmetric nuclear matter (SNM). In doing so, we build on recent results by Tews et al. in Ref. [38], where it was found that the HF energy in PNM for the N^{2}LO 3N forces has a large dependence on the choice of the regulator function. We emphasize that we do *not* resolve here the question of how regulator artifacts are absorbed by the implicit renormalization that occurs when constructing realistic interactions; our intent is to describe the origin of these artifacts and stimulate further investigations.

When studying the effects of the regulators on the energy, we make extensive use of decomposing the NN/3N contributions into their direct and exchange components. While the individual pieces in this decomposition are not physical, it is useful to isolate effects of the regulator on the different sectors of the potential. As an example, certain parts of the N^{2}LO 3N forces (the c_4, c_D, c_E terms) vanish in a system of only neutrons [39]. However, the vanishing for the c_D, c_E components is presupposed on a complete cancellation between the different 3N antisymmetric components. Some regulator choices alter this cancellation by regulating direct and exchange terms differently, resulting in non-zero c_D, c_E contributions even in a pure neutron system[1].

In all cases, our strategy is to analyze the effects of introducing the regulator by considering the interaction phase space, which provides the dominant influence on the energy integrand at a given order in MBPT (and the other parts of the integrand are readily approximated). Except for the simple case of NN HF, the analytic reduction of MBPT integrals is quite cumbersome and the resulting expressions not enlightening. Instead, we propose analyzing momentum-space histograms that are Monte Carlo samplings of the relevant momenta. These histograms denote where the primary strength is located in the energy integrands. How they are constructed will be explained in Section III below.

The plan of the paper is as follows. In Section II we review the chiral interactions at LO and N^{2}LO for the NN and 3N forces, respectively, and define a range of regulators that have been chosen for calculations in each sector. In Section III we analyze the energy contributions at first and second order in MBPT using different combinations of forces and regulators. Section IV then concludes with a summary and future issues that need to be examined.

II. NN/3N CHIRAL FORCES AND REGULATORS

A. LO NN Forces

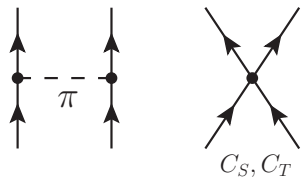

FIG. 1. The leading order chiral NN forces [1, 2].

[1] The c_4 term vanishes due to its isospin structure and not due to an antisymmetric cancellation. As a result the c_4 term is always zero in PNM.

The NN forces at leading-order (LO) in the chiral expansion [1, 2] are sufficiently general for our first look at regulator artifacts in that they contain both long-range and short-range pieces. At lowest order, there are two independent contact terms with LECs C_S, C_T and a static one-pion exchange (OPE) diagram (see Fig. 1), so the potential in momentum space can be written:

$$V_{\rm LO}^{\rm NN} = V_{\rm c}^{\rm NN} + V_{\pi}^{\rm NN} \ , \tag{1a}$$

where

$$V_{\rm c}^{\rm NN} = C_S + C_T(\boldsymbol{\sigma}_1 \cdot \boldsymbol{\sigma}_2) \ , \tag{1b}$$

$$V_{\pi}^{\rm NN}(\mathbf{q}) = -\frac{g_A^2}{4F_\pi^2}\frac{(\boldsymbol{\sigma}_1 \cdot \mathbf{q})\,(\boldsymbol{\sigma}_2 \cdot \mathbf{q})}{q^2+m_\pi^2}\boldsymbol{\tau}_1 \cdot \boldsymbol{\tau}_2 \ . \tag{1c}$$

In terms of incoming (outgoing) single-particle momenta $\mathbf{p}_1, \mathbf{p}_2$ $(\mathbf{p}_1', \mathbf{p}_2')$, the momentum transfer $\mathbf{q}$ and the relative momentum $\mathbf{k}$ (for later use) are

$$\mathbf{q} \equiv \mathbf{p}_1 - \mathbf{p}_1' = \mathbf{p}_2' - \mathbf{p}_2 \ , \quad \mathbf{k} \equiv \frac{\mathbf{p}_1 - \mathbf{p}_2}{2} \ . \tag{2}$$

For all calculations in this paper, the axial coupling constant $g_A = 1.267$ is used along with $C_S = 1.0$ MeV^{-2}.

Because nucleons are fermions, our potentials need to be antisymmetric under particle exchange. To this end, we define the antisymmetrizer A_{12}

$$A_{12} \equiv (1 - P_{12}), \tag{3}$$

where P_{12} is the exchange operator for particles 1 and 2. At HF and 2nd order, expressions with an even number of exchange operators are dubbed "direct" diagrams while expressions with an odd number of exchange operators are called "exchange" diagrams.

The static OPE potential can also be separated in momentum space into two different terms, long-range (LR) and short-range (SR)[2],

$$V_{\pi}^{\rm NN}(\mathbf{q}) = V_{\pi,{\rm LR}}^{\rm NN}(\mathbf{q}) + V_{\pi,{\rm SR}}^{\rm NN}(\mathbf{q}) \ , \tag{4a}$$

where

$$V_{\pi,{\rm LR}}^{\rm NN}(\mathbf{q}) = -\frac{g_A^2}{12F_\pi^2}\left[\frac{q^2\ S_{12}(\hat{\mathbf{q}})}{q^2+m_\pi^2} - \frac{m_\pi^2 \boldsymbol{\sigma}_1 \cdot \boldsymbol{\sigma}_2}{q^2+m_\pi^2}\right]\boldsymbol{\tau}_1 \cdot \boldsymbol{\tau}_2 \ , \tag{4b}$$

$$V_{\pi,{\rm SR}}^{\rm NN}(\mathbf{q}) = -\frac{g_A^2}{4F_\pi^2}\frac{\boldsymbol{\sigma}_1 \cdot \boldsymbol{\sigma}_2}{3}\boldsymbol{\tau}_1 \cdot \boldsymbol{\tau}_2 \ . \tag{4c}$$

The tensor operator $S_{12}(\hat{\mathbf{q}})$ defined as,

$$S_{12}(\hat{\mathbf{q}}) \equiv 3(\boldsymbol{\sigma}_1 \cdot \hat{\mathbf{q}})(\boldsymbol{\sigma}_2 \cdot \hat{\mathbf{q}}) - \boldsymbol{\sigma}_1 \cdot \boldsymbol{\sigma}_2 \ , \tag{4d}$$

where $\hat{\mathbf{q}}$ denotes the momentum transfer unit vector and $q \equiv |\mathbf{q}|$. The above separation corresponds to subtracting off the short-range contact part of the OPE potential.

By taking the Fourier transform of $V_\pi(\mathbf{q})$ in (1c), we can express the OPE potential in coordinate space:

$$V_{\pi}^{\rm NN}(\mathbf{r}) = V_{\pi,{\rm LR}}^{\rm NN}(\mathbf{r}) + V_{\pi,{\rm SR}}^{\rm NN}(\mathbf{r}) \ , \tag{5a}$$

where

$$V_{\pi,{\rm LR}}^{\rm NN}(\mathbf{r}) = \frac{g_A^2}{4F_\pi^2}\frac{m_\pi^2}{12\pi}\frac{e^{-m_\pi r}}{r} \times \left[\left(1 + \frac{3}{m_\pi r} + \frac{3}{(m_\pi r)^2}\right) S_{12}(\hat{\mathbf{r}}) + \boldsymbol{\sigma}_1 \cdot \boldsymbol{\sigma}_2\right]\boldsymbol{\tau}_1 \cdot \boldsymbol{\tau}_2 \ , \tag{5b}$$

$$V_{\pi,{\rm SR}}^{\rm NN}(\mathbf{r}) = -\frac{g_A^2}{12F_\pi^2}\delta^3(\mathbf{r})\boldsymbol{\sigma}_1 \cdot \boldsymbol{\sigma}_2\ \boldsymbol{\tau}_1 \cdot \boldsymbol{\tau}_2 \ . \tag{5c}$$

Here r denotes the magnitude of the relative distance and $\hat{\mathbf{r}}$ is its unit vector. As before, the potential can be separated into a short-range contact part along with long-range central and tensor contributions.

In the following, we work exclusively with the long-range part of the OPE potential. That is to say, by OPE we are referring *only* to $V_{\pi,{\rm LR}}^{\rm NN}(\mathbf{q})$ in (4b) for momentum space and $V_{\pi,{\rm LR}}^{\rm NN}(\mathbf{r})$ in (5b) for coordinate space. Including the contact part of OPE is superfluous for our purposes as its behavior under regularization is the same as for the C_S, C_T terms. Furthermore, absorbing the OPE delta function into the leading-order contact avoids mixing contact regularization effects with the remaining central and tensor parts of the OPE potential. Explicitly separating out the delta function from the OPE potential is standard practice for potentials regulated in coordinate space.

For energies to be finite at second-order in MBPT, a regularization scheme must be introduced. For a general local NN potential, there will only be one independent momentum that needs to be regulated after taking momentum conservation into consideration. Regulators in general can either be local or nonlocal. By definition, local regulators (and potentials) are functions purely of the relative distance $\mathbf{r}$ in coordinate space or the momentum transfer $\mathbf{q}$ in momentum space. Nonlocal regulators (and potentials) have additional dependencies other than just $\mathbf{r}$ or $\mathbf{q}$.

One popular choice is a nonlocal regulator, which we call momentum space nonlocal (MSNL), defined to exponentially regulate the relative momentum magnitude k [32, 39, 40],

$$f_{\rm MSNL}^{\rm NN}(k^2) = \exp\left[-\left(k^2/\Lambda_{\rm NN}^2\right)^n\right] \ , \tag{6}$$

where $\Lambda_{\rm NN}$ is the NN cutoff in momentum space and n is a fixed integer. For current NN calculations, typical values include $n = 1-3$ and $\Lambda_{\rm NN} = 450-$

[2] The terminology long-range and short-range is somewhat a misnomer here. It is used for convenience to distinguish the contact part of the OPE potential. The long-range part of the OPE still has 'short-range' components, i.e., a $1/r^3$ term in the tensor.

600 MeV [33, 39, 41]. The relative momentum magnitudes both before and after the interaction are regulated to satisfy hermiticity, so the potential assumes the form:

$$V^{\rm NN}(\mathbf{k},\mathbf{k}') \implies f^{\rm NN}_{\rm MSNL}(k^2)\, V^{\rm NN}(\mathbf{k},\mathbf{k}')\, f^{\rm NN}_{\rm MSNL}(k'^2)\,, \tag{7}$$

where $\mathbf{k}\,(\mathbf{k}')$ denotes the relative momentum before (after) the interaction. These regulators are symmetric under individual nucleon permutation so that direct and exchange pieces of the antisymmetric potential are regulated identically. Under a partial wave decomposition of the potential, all waves are also cut off in the same way. Figure 2 shows the effect of different values of n (e.g., on a diagonal potential in Eq. (7)), which can be compared to the $n \to \infty$ limit of a step function at $k = \Lambda_{\rm NN}$.

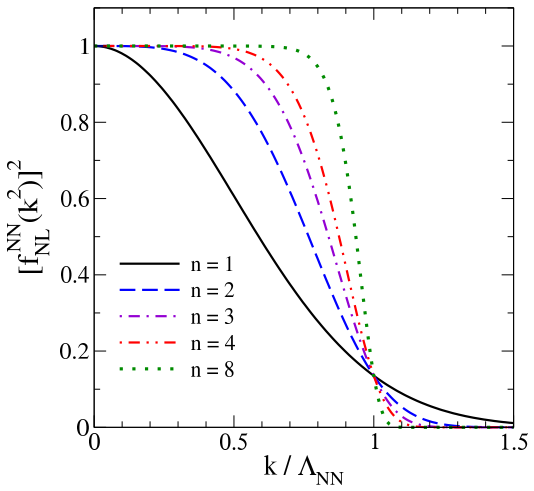

FIG. 2. Examples of different choices of n, from 1 to 8, in the nonlocal regulator exponential of Eq. (6). The x-axis is the magnitude of the relative momentum scaled by the cutoff and the y-axis is the regulator function squared.

A different approach is to use a local regulator, which we call momentum space local (MSL), that depends on the momentum transfer magnitude q, as in Ref. [30],

$$f^{\rm NN}_{\rm MSL}(q^2) = \exp\left[-\left(q^2/\Lambda^2_{\rm NN}\right)^n\right]\,, \tag{8}$$

such that,

$$V^{\rm NN}(\mathbf{q}) \implies V^{\rm NN}(\mathbf{q}) f^{\rm NN}_{\rm MSL}(q^2)\,, \tag{9}$$

where we have written the NN potential in local form as a pure function of $\mathbf{q}$. As the regulator in (8) is not symmetric under single-particle permutation, the direct and exchange parts of the potential are not regulated in the same way. Likewise, different partial waves will experience different cutoff artifacts.

An alternative local approach is to regulate in coordinate space on the magnitude of the relative distance r with some coordinate space cutoff R_0. Depending on the exponent n, these regulators may have oscillatory behavior when transformed to momentum space and display different behavior from local momentum space regulators. For the coordinate-space regulated OPE, these different regularization schemes have the least effect in high partial waves because one is cutting off short-distance (small r) parts of the potential. A fully local choice used in some quantum Monte Carlo calculations, which we label CSL, is to use [42],

$$f^{\rm NN}_{\rm CSL}(r^2) = \left(1 - \exp\left[-\left(r^2/R_0^2\right)^n\right]\right)\,, \tag{10}$$

to regulate the long-range part of the OPE potential,

$$V^{\rm NN}_{\pi,\rm LR}(\mathbf{r}) \implies V^{\rm NN}_{\pi,\rm LR}(\mathbf{r})\, f^{\rm NN}_{\rm CSL}(r^2)\,, \tag{11}$$

which cuts off the short distance (small r) parts of the OPE potential [33]. The short-range contacts and short-range OPE are regulated by replacing the Dirac delta function with a smeared delta function [36, 42],

$$\delta(\mathbf{r}) \to \delta_{R_0}(\mathbf{r}) = \alpha_n e^{-(r^2/R_0^2)^n}\,, \tag{12}$$

where α_n is a normalization coefficient, chosen such that

$$\int d^3r\; \delta_{R_0}(\mathbf{r}) = 1\,. \tag{13}$$

It is also possible to mix local and nonlocal forms. One semi-local choice developed by Epelbaum, Krebs, and Meißner, which we label EKM, is to use [33]

$$f^{\rm NN}_{\rm EKM}(r^2) = \left(1 - \exp\left[-\left(r^2/R_0^2\right)\right]\right)^n\,, \tag{14}$$

for the long-range OPE potential,

$$V^{\rm NN}_{\pi,\rm LR}(\mathbf{r}) \implies V^{\rm NN}_{\pi,\rm LR}(\mathbf{r})\, f^{\rm NN}_{\rm EKM}(r^2)\,, \tag{15}$$

and use (6) on the short-range contacts (and short-range OPE). The EKM long-range regularization is sufficient to make the previously used spectral function regularization of the highly singular TPE potential unnecessary for $n \geq 4$ [33]. Current NN implementations use $R_0 = 0.8 - 1.2$ fm as typical cutoffs [43].

The different NN regulator schemes used in this paper are summarized in Table I. We note that the momentum-space regulator functions MSNL and MSL are constructed such that they approach one as their

TABLE I. Summary table for various regulator combinations in the NN sector defined in the text, with equation references to the regulators in parenthesis. OPE refers to (4b) in momentum space and (5b) in coordinate space. Contacts refers to both the C_S, C_T terms along with the OPE contact in (4c) and (5c).

Scheme	Type	OPE	Contacts
MSNL	nonlocal	nonlocal (6)	nonlocal (6)
MSL	local	local (8)	local (8)
EKM	semi-local	local (14)	nonlocal (6)
CSL	local	local (10)	local (12)

momentum arguments go to zero. This is not true for the coordinate-space local regulators used in EKM and CSL. However, these regulators preserve the strength of the OPE potential at the pion pole, as has been typically required for form factors used with phenomenological potentials (e.g., see Ref. [44]).

B. N^{2}LO 3N Forces

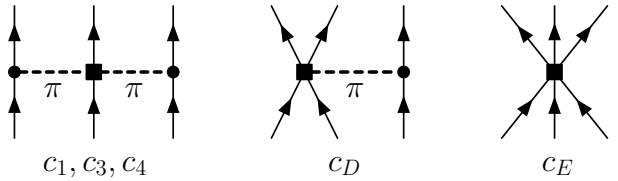

FIG. 3. The N^{2}LO chiral 3N forces [1, 2].

The N^{2}LO 3N forces [27, 45] (see also [46]) in the Δ-less χEFT consist of a long-range TPE with c_i coefficients determined from πN scattering, a single-pion exchange with a short-range contact c_D, and a pure contact c_E term (see Fig. 3):

$$V^{\rm 3N}_{\rm N^2LO} = V^{\rm 3N}_{2\pi} + V^{\rm 3N}_{\rm D} + V^{\rm 3N}_{\rm E} \ , \tag{16a}$$

$$V^{\rm 3N}_{2\pi} = \frac{1}{2}\left(\frac{g_A}{2F_\pi}\right)^2 \sum_{i\neq j\neq k} \frac{(\boldsymbol{\sigma}_i\cdot\mathbf{q}_i)\,(\boldsymbol{\sigma}_j\cdot\mathbf{q}_j)}{(q_i^2+m_\pi^2)\,(q_j^2+m_\pi^2)} F^{\alpha\beta}_{ijk}\tau_i^\alpha\tau_j^\beta \ , \tag{16b}$$

$$F^{\alpha\beta}_{ijk} = \delta^{\alpha\beta}\left[-\frac{4c_1m_\pi^2}{F_\pi^2}+\frac{2c_3}{F_\pi^2}\mathbf{q}_i\cdot\mathbf{q}_j\right] + \sum_\gamma \frac{c_4}{F_\pi^2}\epsilon^{\alpha\beta\gamma}\tau_k^\gamma\boldsymbol{\sigma}_k\cdot(\mathbf{q}_i\times\mathbf{q}_j) \ , \tag{16c}$$

$$V^{\rm 3N}_{\rm D} = -\frac{g_A}{8F_\pi^4}\frac{c_D}{\Lambda_\chi}\sum_{i\neq j\neq k}\frac{(\boldsymbol{\sigma}_j\cdot\mathbf{q}_j)\,(\boldsymbol{\sigma}_i\cdot\mathbf{q}_j)}{q_j^2+m_\pi^2}\boldsymbol{\tau}_i\cdot\boldsymbol{\tau}_j \ , \tag{16d}$$

$$V^{\rm 3N}_{\rm E} = \frac{c_E}{2F_\pi^4\Lambda_\chi}\sum_{j\neq k}(\boldsymbol{\tau}_j\cdot\boldsymbol{\tau}_k) \ , \tag{16e}$$

where the subscripts i,j,k are particle indices.[3] For all calculations in this paper, $c_i = 1.0$ GeV^{-1}, $c_D = 1.0$, $c_E = 1.0$.

As in the 2-body sector we define an antisymmetrizer A_{123} to ensure that our 3N potential is antisymmetric under particle exchange,

$$A_{123} \equiv (1-P_{12})(1-P_{13}-P_{23}) \ . \tag{17}$$

[3] Note that the Λ_χ appearing in the 3N potentials is distinct from $\Lambda_{\rm NN}$ and $\Lambda_{\rm 3N}$. Λ_χ denotes the estimated breakdown scale of χEFT while $\Lambda_{\rm NN}$ and $\Lambda_{\rm 3N}$ come purely from regulating the EFT.

Depending on the number of exchange operators in our energy expressions, we have "direct", "single-exchange", and "double-exchange" diagrams.

For calculations to be finite past first order in perturbation theory, we again need to introduce a regularization scheme for our 3-body potentials. For a local 3N potential, there will in general be 2 independent momenta after momentum conservation. One commonly used choice is a nonlocal regulator completely symmetric in the single-particle momenta,

$$f^{\rm 3N}_{\rm MSNL}(\mathbf{p}_1,\mathbf{p}_2,\mathbf{p}_3) = \exp\left[-\left(\frac{p_1^2+p_2^2+p_3^2-\mathbf{p}_1\cdot\mathbf{p}_2-\mathbf{p}_1\cdot\mathbf{p}_3-\mathbf{p}_2\cdot\mathbf{p}_3}{3\Lambda^2_{\rm 3N}}\right)^n\right], \tag{18}$$

which we call MSNL. Like its 2-body nonlocal counterpart, this regulator retains its functional form under permutation of the nucleon indices and thus regulates each antisymmetric piece of the 3-body potential in the same way. The nonlocal regulator can be equivalently written in terms of the magnitudes of the 3-body Jacobi momenta,

$$f^{\rm 3N}_{\rm MSNL}(k^2,j^2) = \exp\left[-\left(\frac{k^2+\frac{3}{4}j^2}{\Lambda^2_{\rm 3N}}\right)^n\right], \tag{19}$$

where we define the Jacobi momenta $\mathbf{j},\mathbf{k}$ with respect to the $1,2$ particle subsystem,

$$\mathbf{j} = \frac{2}{3}\left(\mathbf{p}_3 - \frac{\mathbf{p}_2+\mathbf{p}_1}{2}\right) \ , \qquad \mathbf{k} = \frac{\mathbf{p}_2-\mathbf{p}_1}{2} \ . \tag{20}$$

To satisfy hermiticity, again we regulate on both the incoming and outgoing Jacobi momenta,

$$V^{\rm 3N}(\mathbf{j}',\mathbf{k}';\mathbf{j},\mathbf{k}) \implies f^{\rm 3N}_{\rm MSNL}(k'^2,j'^2)\ V^{\rm 3N}(\mathbf{j}',\mathbf{k}';\mathbf{j},\mathbf{k})\ f^{\rm 3N}_{\rm MSNL}(k^2,j^2) \ . \tag{21}$$

Common choices for the 3N MSNL regulator include $n = 2-3$ and $\Lambda_{\rm 3N} = 400-600$ MeV [15, 45, 47]. Usually $\Lambda_{\rm 3N}$ is chosen to be equal to $\Lambda_{\rm NN}$, but the necessity for this has not been established.

Another choice, which we dub MSL, is the Navratil local regulator defined as [48],

$$f^{\rm 3N}_{\rm MSL}(q_i^2) = \exp\left[-\left(\frac{\mathbf{q}_i^2}{\Lambda^2_{\rm 3N}}\right)^n\right] \ , \tag{22}$$

where e.g., $\mathbf{q}_1 = \mathbf{p}_1 - \mathbf{p}_1'$ is the momentum transfer in terms of individual nucleon three-momenta with $\mathbf{p}_1$ ($\mathbf{p}_1'$) being the momenta before (after) the interaction. The 3N potential expressed in local form after regularization becomes,

$$V^{\rm 3N}(\mathbf{q}_i,\mathbf{q}_j) \implies f^{\rm 3N}_{\rm MSL}(q_i^2)\ V^{\rm 3N}(\mathbf{q}_i,\mathbf{q}_j)\ f^{\rm 3N}_{\rm MSL}(q_j^2) \ , \tag{23}$$

where the subscripts i,j refer to momentum transfers between different single-particle momenta. Like the local momentum space regulator in (8), the Navratil local regulator is not symmetric under individual nucleon

permutations. As such, the different parts of the fully antisymmetric 3N potential are all regulated differently. This also results in ambiguities in deciding how to regulate different parts of the long-range 3N forces depending on if the regulator momentum labels i, j match the spin-isospin labels in the 3N potential [38, 48, 49]. Taking the potential V_D^{3N} with LEC c_D as an example, we denote below two different regularization structures following Ref. [48],

$$f^{3N}_{MSL}(q_i^2)\ \frac{(\boldsymbol{\sigma}_j\cdot\mathbf{q}_j)\,(\boldsymbol{\sigma}_i\cdot\mathbf{q}_j)}{q_j^2+m_\pi^2}\ \boldsymbol{\tau}_i\cdot\boldsymbol{\tau}_j\ f^{3N}_{MSL}(q_j^2)\ , \tag{24a}$$

$$f^{3N}_{MSL}(q_k^2)\ \frac{(\boldsymbol{\sigma}_j\cdot\mathbf{q}_j)\,(\boldsymbol{\sigma}_i\cdot\mathbf{q}_j)}{q_j^2+m_\pi^2}\ \boldsymbol{\tau}_i\cdot\boldsymbol{\tau}_j\ f^{3N}_{MSL}(q_j^2)\ . \tag{24b}$$

The momentum transfer labels in the regulators match the spin-isospin indices in (24a), whereas only one index is matched in (24b). In this paper, for the purposes of calculation, we adopt the convention of Eq. (24b).

III. RESULTS

To explore the regulator dependence in χEFT, we study the uniform system (infinite, homogeneous, isotropic matter) in MBPT. The uniform system has the desirable feature that certain non-perturbative aspects of nuclear systems in free-space, e.g., the fine-tuning of the NN S-waves, are rapidly damped at finite density [50]. In this paper, with the exception of 3N second-order, we work exclusively with PNM up to the first two orders in MBPT. This is because PNM is simpler and more perturbative than SNM and serves as a testbed without the complications of including isospin. In test cases, we have found similar trends in these two limiting systems.

In the following, we look first at the NN forces at HF and second-order in MBPT, then we examine 3N forces in the same sequence. Examining both the HF and the second-order energy allows the probing of different parts of the nuclear potentials with a regulator scheme. The HF energy has the feature of being computable without a regulator and serves as a touchstone for examining scheme/scale dependence. As all HF momenta are on-shell, regulator effects here are described as IR effects. The second-order energy is divergent in the absence of regularization, hence artifacts from the regulator here are called UV effects.

A. NN Forces at HF

For a 2-body interaction, the HF energy per particle in terms of single-particle momenta is given by

$$\frac{E^{NN}_{HF}}{N}=\frac{1}{2\rho}\sum_{\sigma_1,\sigma_2}\sum_{\tau_1,\tau_2}\int\frac{d^3p_1}{(2\pi^3)}\int\frac{d^3p_2}{(2\pi)^3}\times n(\mathbf{p}_1)n(\mathbf{p}_2)\langle 12|A_{12}V^{NN}_{LO}|12\rangle\ , \tag{25}$$

where

$$|1\rangle\equiv|\mathbf{p}_1\sigma_1\tau_1\rangle, \tag{26a}$$

$$n(\mathbf{p}_1)\equiv\Theta(\,k_F-|\mathbf{p}_1|), \tag{26b}$$

ρ is the nucleon number density, σ_i (τ_i) is the spin (isospin) operator for the ith particle, and V^{NN}_{LO} are the LO chiral NN forces with a particular regularization scheme.

Evaluating the HF energy using the different regulator schemes in Table I yields the curves in Fig. 4 for the C_S and OPE terms. At this stage we have already separated the direct and exchange parts of the potential, $\langle 12|V^{NN}_{LO}|12\rangle$ and $\langle 12|V^{NN}_{LO}|21\rangle$ respectively, to illustrate differences in regulator behavior on energy calculations. Note that there is no direct OPE energy as spin-isospin dependent interactions at HF vanish when performing spin-isospin traces. Calculations are presented here for soft cutoffs of $\Lambda_{NN}=2.0$ fm^{-1} and $R_0=1.2$ fm to better highlight regulator artifacts at high density. Performing calculations at a more common $\Lambda_{NN}=2.5$ fm^{-1} or $R_0=0.9$ fm does not alter our qualitative discussion below (see supplemental material). The regulator situation at HF is particularly simple and our analysis in this section serves as a proof of principle of how our various diagnostic tools can explain the systematics of the energy.

The unregulated direct C_S HF energy in Fig. 4(a) is exactly reproduced for the MSL and CSL regulator schemes because $\mathbf{q}=0$ for the direct diagram. In contrast, the MSNL result is suppressed. The exchange C_S HF energy shows a different hierarchy where, in order of absolute magnitude, one finds MSNL > CSL $\sim$ MSL.

The exchange C_S HF energies in Fig. 4(b) imply that the CSL contact regulator in (12) has similar behavior to the MSL regulator in (8) for the cutoffs $\Lambda_{NN}=2.0$ fm^{-1} and $R_0=1.2$ fm. In the special case of $n=1$ with a no-derivative contact, a straightforward Fourier transform connects these two regulators, i.e.,

$$\begin{aligned}\mathcal{F}\left[V^{NN}_{C_S}\ f^{NN}_{MSL}(q^2)\right]&=C_S\int\frac{d^3q}{(2\pi)^3}e^{i\mathbf{q}\cdot\mathbf{r}}\ e^{-q^2/\Lambda^2_{NN}}\\&=C_S\alpha_1\ e^{-r^2/R_0^2}\end{aligned} \tag{27}$$

where $R_0=2/\Lambda_{NN}$ and $\alpha_1=(R_0^3\ \pi^{3/2})^{-1}$. Only for this special case will the regulators be directly related. At larger n, the relations become more complicated hypergeometric functions and the correspondence between Λ_{NN} and R_0 is no longer clean. We plot the choice of $n=2$ for contact CSL and MSL in Fig. 5(a) to illustrate this different behavior. The oscillatory nature of the Fourier transformed regulator implies that no simple redefinition of Λ_{NN} or R_0 will completely equate the two regulators.

For the exchange OPE, the hierarchy in energy values in Fig. 4(c), in decreasing order of magnitude, is MSNL > MSL > CSL > EKM. The significant deviation in the

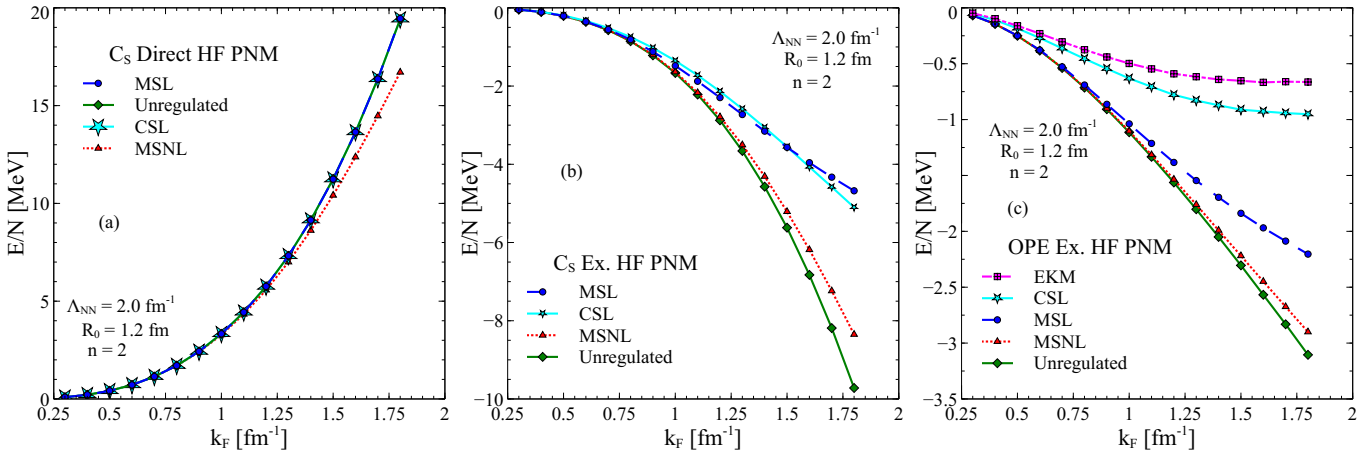

FIG. 4. Neutron matter calculations of the HF energy per particle for the direct (a) and exchange (b) terms for C_S and the OPE exchange term (c) using the regularization schemes in Table I. The C_T calculation has similar behavior to the C_S exchange term. The EKM scheme uses the same regularization as the MSNL scheme for the contact terms. The trends in SNM (not shown) are comparable to those in PNM. The calculations use $n = 2$, $\Lambda_{\rm NN} = 2.0$ fm^{-1}, and $R_0 = 1.2$ fm.

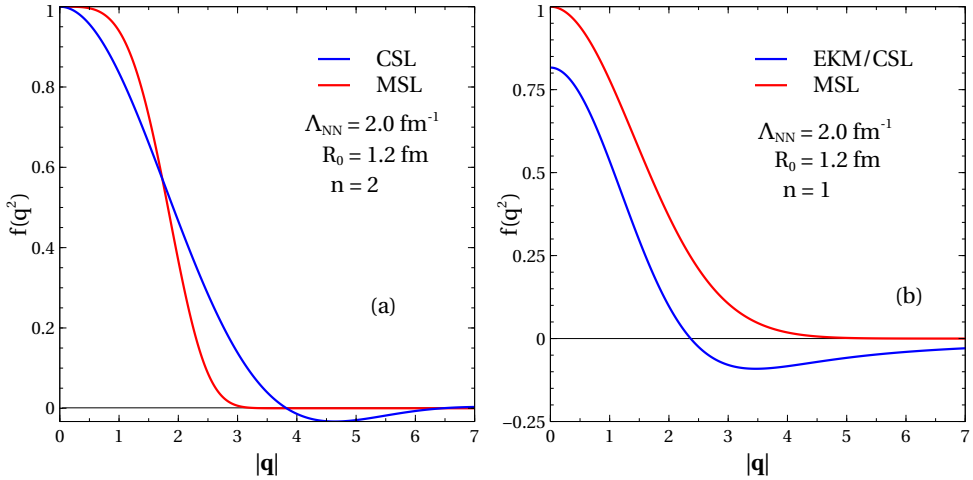

FIG. 5. Plot (a) shows the MSL regulator in (8) and CSL contact regulator in (12) for $n = 2$, $R_0 = 1.2$ fm, $\Lambda_{\rm NN} = 2.0$ fm^{-1}. Plot (b) shows the MSL regulator in (8) and CSL/EKM OPE regulator in (10) or (14) for $n = 1$, $R_0 = 1.2$ fm, $\Lambda_{\rm NN} = 2.0$ fm^{-1}. The regulator function is plotted as a function of the momentum transfer magnitude $|\mathbf{q}|$. The S_{12} operator, which vanishes for HF, was set to zero before performing the Fourier transform for EKM/CSL. Hence the OPE EKM/CSL regulator functional form as plotted is valid for HF only.

MSL, EKM, and CSL OPE energies compared to unregulated HF can be traced to the regulation of the small r parts of the OPE potential. The energy density of uniform nuclear matter is dominated by the low partial waves (e.g., S,P,D waves). The MSL, CSL, and EKM regulators, in (8), (10), and (14) respectively, by construction cut off the potential at small r and will thus affect these low partial waves to a greater extent than the MSNL scheme.

The energy trends in the graphs of Fig. 4 are directly linked to the interaction phase space, as we now demonstrate. This is most apparent for a sharp regulator, for which five of the six integrals in (25) can be done analytically for pure S-wave or contact potentials. Dropping prefactors, we find the phase space is proportional to the dimensionless integrand [51, 52],

$$\left(\frac{k}{k_{\rm F}}\right)^2 \left(2 - 3\frac{k}{k_{\rm F}} + \left(\frac{k}{k_{\rm F}}\right)^3\right) f_{\rm reg} \ , \qquad (28)$$

where $f_{\rm reg}$ refers generically to any regularization scheme. We have also suppressed the overall dependence on $k_{\rm F}$ and the potential. Making the MSNL regulator in (6) sharp results in,

$$f^{\rm NN}_{\rm MSNL}(k^2) \xrightarrow[n\to\infty]{} \Theta\left(\frac{\Lambda_{\rm NN} - k}{k_{\rm F}}\right) \qquad (29)$$

while making the MSL regulator in (8) sharp gives different results for direct and exchange terms due to regu-

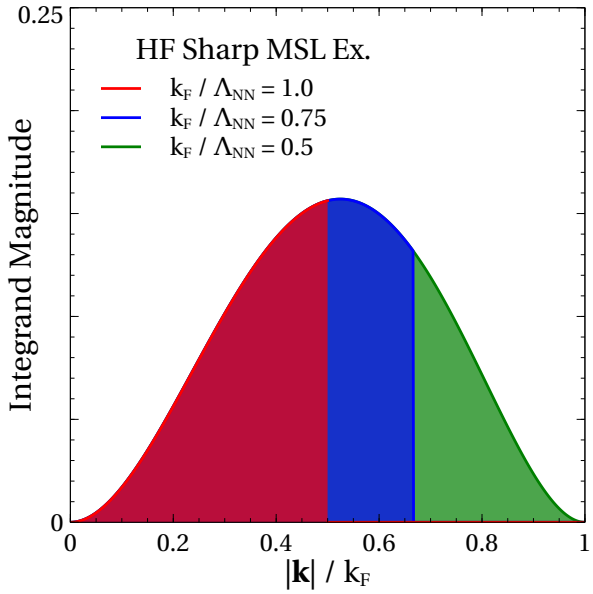

FIG. 6. Phase space of the Hartree-Fock exchange term regulated with the sharp MSL regulator of (30). The magnitude of the dimensionless integrand in (28) is plotted as a function of $k/\,k_{\rm F}$. The colored regions indicate the phase space included for different values of $k_{\rm F}/\Lambda_{\rm NN}$.

lating in the momentum transfer,

$$f^{\rm NN}_{\rm MSL}(q^2) \xrightarrow[n\to\infty]{} \mathbf{1} \qquad \text{Direct,}$$
$$f^{\rm NN}_{\rm MSL}(q^2) \xrightarrow[n\to\infty]{} \Theta\left(\frac{\Lambda_{\rm NN}-2k}{k_{\rm F}}\right) \qquad \text{Exchange .} \quad (30)$$

Therefore, for a sharp cutoff chosen above the Fermi surface $k_{\rm F}$, the HF phase space will be unaltered by the MSNL regulator. In contrast, the exchange term regulated in the sharp MSL scheme gets cut off as soon as $k_{\rm F}/\Lambda_{\rm NN} > 0.5$ (i.e., the effective cutoff in the MSL exchange case is half that in the MSNL case). This is shown in Fig. 6, where the colored region indicates the integration region for different values of $k_{\rm F}/\Lambda_{\rm NN}$. For example, for $k_{\rm F}/\Lambda_{\rm NN} = 1.0$ all the phase space above $k/\,k_{\rm F} = 0.5$ has been completely removed by the sharp MSL regulator while for $k_{\rm F}/\Lambda_{\rm NN} = 0.5$, the full phase space is still extant. As a result, in regions where the Fermi momentum is small compared with the cutoff, we expect little deviation between the unregulated, MSNL, and MSL HF energy.

Although at HF the phase space in (28) can be analytically derived, the situation is considerably more complicated at second-order and in the 3-body sector. In anticipation of this, we develop a new way to visualize the regulator phase space occlusion using a diagnostic based on Monte Carlo sampling. To understand regulator effects and the hierarchy of energy values, we propose creating plots of the HF integrand in (25) and plotting it against the relative momentum magnitude as is done in Fig. 7. These histogram plots will be the main analysis tool for regulator effects on the potential both at HF and at higher orders in perturbation theory. They are created by randomly generating single-particle momenta $\mathbf{p}_1, \mathbf{p}_2$ by Monte Carlo sampling and then calculating the scaled HF energy integrand I_1,

$$I_1 = |f_{\rm reg}|\,\frac{k^2}{k_{\rm F}^2}\,\frac{P^2}{k_{\rm F}^2}\,n(\mathbf{P}/2+\mathbf{k})\,n(\mathbf{P}/2-\mathbf{k}) \times \begin{cases} 1, & \text{Contact} \\ \dfrac{m_\pi^2}{q^2+m_\pi^2}\,, & \text{OPE} \end{cases} \quad (31)$$

where $f_{\rm reg}$ refers to a regularization scheme in Table I, $\mathbf{P}$ is the total momentum, $\mathbf{P} = \mathbf{p}_1 + \mathbf{p}_2$, and the integrand is weighted by a contact or OPE interaction[4]. The value of the integrand I_1 is then binned for the corresponding relative momentum magnitude k (normalized by $k_{\rm F}$) and the process is repeated. After a sufficiently high number of momenta are generated, the final plot is normalized by the total number of iterations. The scaling of the momentum magnitudes k and P by $k_{\rm F}$ is done here for convenience.

These histograms can be interpreted as the phase space available to the system at HF in MBPT now weighted by momenta and the interaction $V^{\rm NN}$. The interaction weighting is included to demonstrate how different interactions weight different parts of the phase space and how this interplays with differing regularization schemes.

We use these plots for three key purposes:

1. to show that the hierarchy in computed MBPT energy values matches the volumes of the weighted phase space,
2. to illuminate where in the phase space different regulators act, i.e., where the contribution to the energy integral becomes small,
3. to demonstrate how different interactions interplay with the regularization schemes.

Addressing these points in order, we first note that the volume of weighted phase space tracked for different regulator choices in Fig. 7 exactly matches the hierarchy in energy values of Fig. 4. For example, the C_S direct energy in Fig. 4(a) is unaltered for the CSL and MSL regulator schemes while the MSNL scheme shows an increasing suppression for increasing $k_{\rm F}$. Looking at Fig. 7(a), the direct C_S histograms show an increasing loss of phase space at large $|\mathbf{k}|/\,k_{\rm F}$ for the MSNL scheme as $k_{\rm F}$ increases while the MSL and CSL phase spaces are unaltered. A corresponding matching of weighted phase space volume to energy calculations exists for the exchange C_S and OPE terms as well. Increasing the integer n in the MSNL and MSL regulators (i.e., making the

[4] The term in (4b) proportional to the S_{12} operator is zero at HF after preforming spin traces.

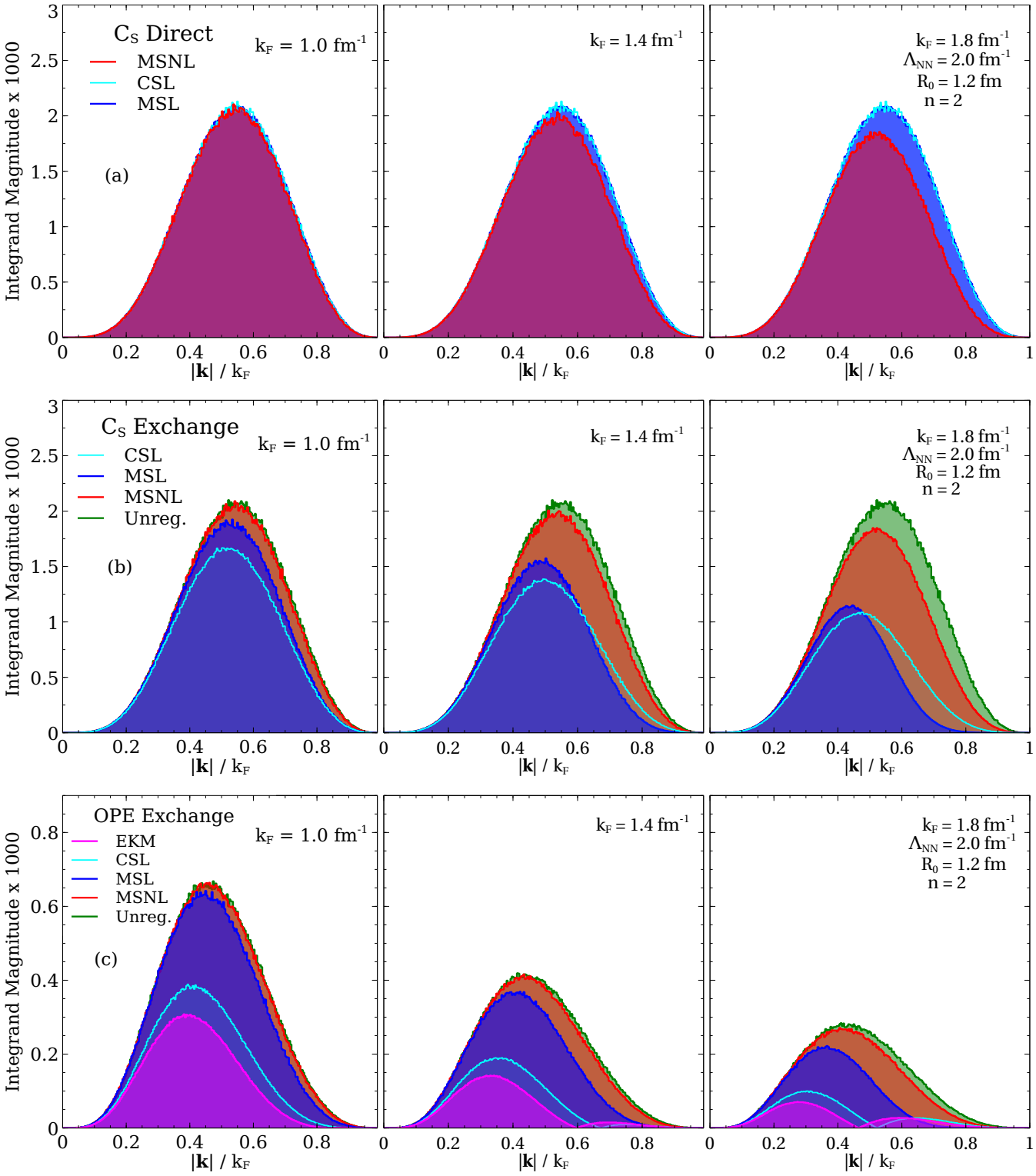

FIG. 7. (color online) Momentum histograms of the 2-body HF integrand for the LO NN forces at $k_F = 1.0$, 1.4, and 1.8 fm^{-1}. The integrand magnitude I_1 in (31) for the direct C_S (a), exchange C_S (b), and exchange OPE (c) is plotted as a function of the dimensionless k/k_F. The integrand magnitude I_1 is also scaled by a factor of 1000. All graphs are evaluated at $\Lambda_{NN} = 2.0$ fm^{-1}, $R_0 = 1.2$ fm, with $n = 2$.

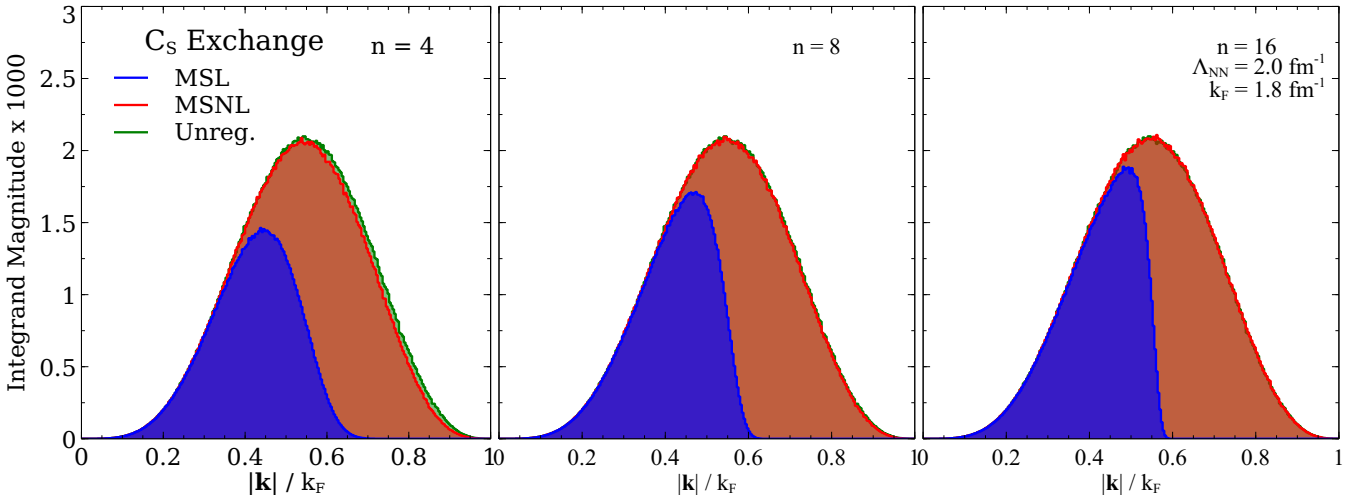

FIG. 8. (color online) Momentum histograms of the 2-body HF integrand for the exchange C_S term at $n = 4$, 8, 16. The integrand magnitude I_1 in (31) is plotted as a function of $k/\,k_{\rm F}$. The integrand magnitude I_1 is also scaled by a factor of 1000. As the exponent n in the regulator is increased, the full phase space is recovered for the MSNL regulator, while the MSL regulator approaches a theta function, in agreement with (29) and (30). All graphs are evaluated at $k_{\rm F} = 1.8$ fm^{-1}, $\Lambda_{\rm NN} = 2.0$ fm^{-1}.

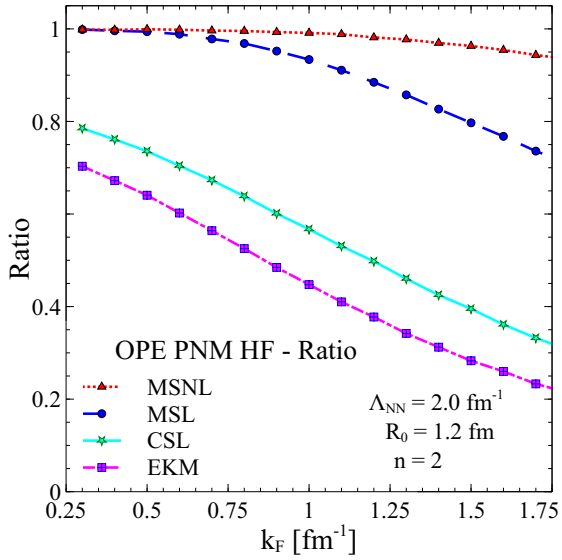

FIG. 9. Ratio of the regulated HF OPE energy in PNM to the unregulated one, as a function of $k_{\rm F}$. Unlike the momentum space regulators, the long-range CSL and EKM regulators do *not* reproduce the full HF energy in the low-density limit. The calculations use $n = 2$, $R_0 = 1.2$ fm, and $\Lambda_{\rm NN} = 2.0$ fm^{-1}.

regulators sharper) for the C_S exchange term at a fixed density results in the plots in Fig. 8. As n increases, one recovers the full space for the MSNL scheme and the sharp cutoff limit for the MSL scheme in agreement with (29) and (30).

Secondly, we see that the primary regions that get suppressed in the weighted phase space, for both the contact and OPE plots, are regions of large $|\mathbf{k}|/\,k_{\rm F}$. This is expected given the form of the MSNL regulator in (6), that all local regulators will suppress large $\mathbf{q}$, and that there is a simple relation between $\mathbf{q}$ and $\mathbf{k}$ at HF,

$$\begin{aligned} \mathbf{q} &= 0 \qquad && \text{Direct}, \\ \mathbf{q} &= 2\mathbf{k} \qquad && \text{Exchange}\,. \end{aligned} \tag{32}$$

As such, how the phase space is cut off for this class of regulators is mostly universal at HF. Note also the interesting behavior in Fig. 7(c) in the OPE case in that both the CSL and EKM phase spaces go to zero at some value of $|\mathbf{k}|/\,k_{\rm F}$ at larger densities ($k_{\rm F} = 1.8$ fm^{-1}) and then increase again. This reflects the oscillatory nature of the Fourier-transformed regulator (see Fig. 5(b)). Fig. 5(b) also reveals that the EKM/CSL regulator function does not approach 1 for $|\mathbf{q}| \to 0$ (while preserving the strength of the OPE potential at the pion pole, as noted at the end of Sec. II A). This can be seen in the modification of the phase space in Fig. 7(c) at low $k/\,k_{\rm F}$. As a consequence, the ratio of the regulated to unregulated HF OPE energy, plotted in Fig. 9, does not go to 1 at low $k_{\rm F}$ for the EKM/CSL regulators.

Thirdly, we can compare the weighted phase space distribution to see the effect of the different interactions, contact vs. OPE[5]. The C_S and OPE plots are very similar to one another suggesting that the regulators are primarily determining the distribution. The key difference between the two is the shifting of the maximum OPE phase space distribution towards smaller $\mathbf{k}$ (cf. the distribution peak in C_S and OPE in Fig. 7 (b) and (c)). This

[5] Note that in scaling the momentum magnitudes k and P by $k_{\rm F}$ in I_1, larger $k_{\rm F}$ will tend to shrink the distribution when weighting by the OPE interaction.

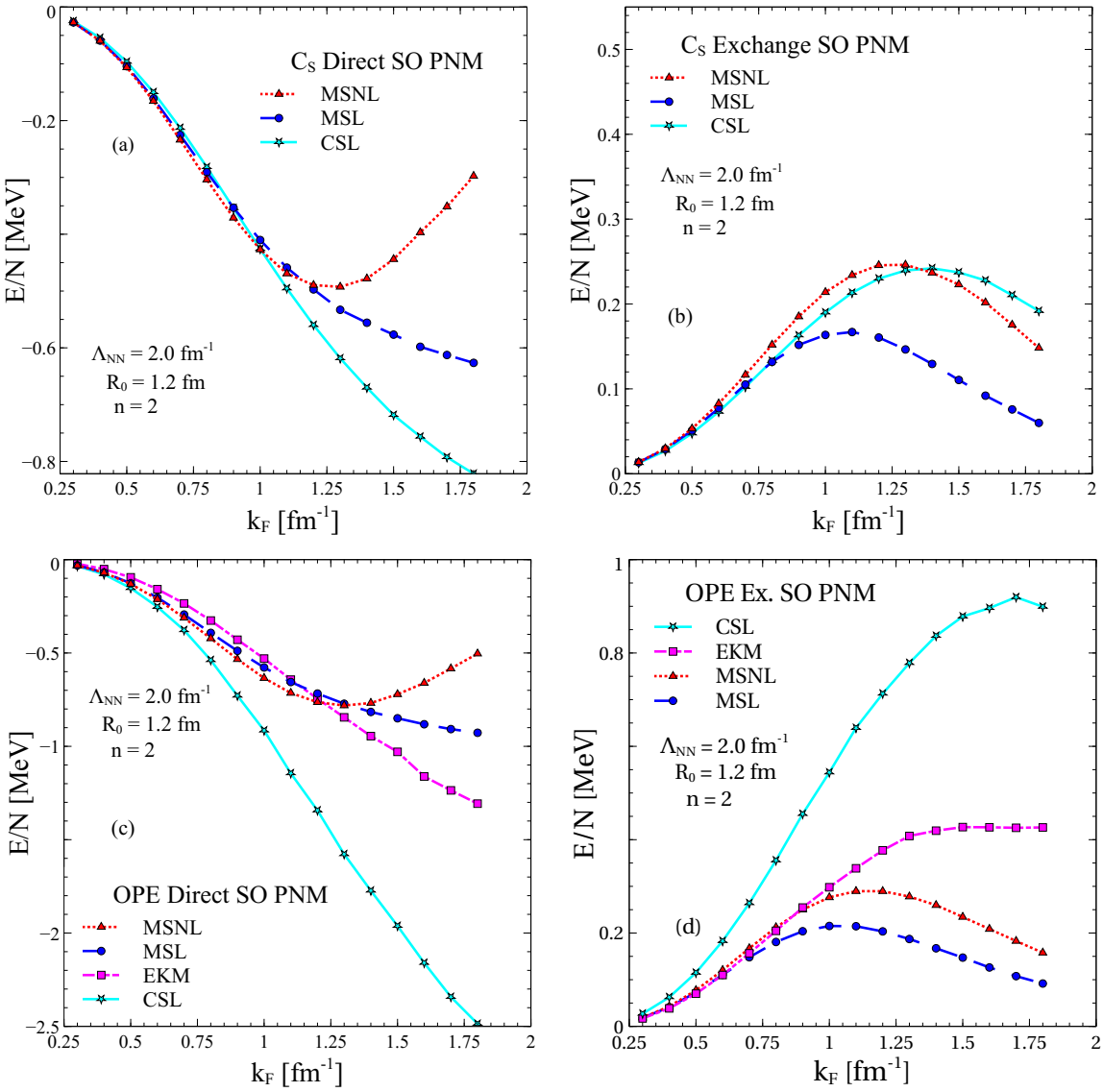

FIG. 10. Neutron matter calculations of the second-order energy for the C_S–C_S direct (a) and exchange (b) terms along with the OPE–OPE direct (c) and exchange (d) terms using different regulators. The calculations are done at $\Lambda_{\rm NN} = 2.0$ fm^{-1}, $R_0 = 1.2$ fm, and $n = 2$.

shifting of the peak of the OPE phase space distribution results in less suppression for the regulated energy values, as can be seen in comparing the OPE and C_S exchange energies in Fig. 4 (b) and (c).

B. NN Forces at Second-Order

For a 2-body interaction at second-order in MBPT, the energy per particle in terms of single-particle momenta is,

$$\frac{E^{\rm NN}_{\rm SO}}{N} = \frac{1}{4\rho}\left[\prod_{i=1}^{4}\sum_{\sigma_i}\sum_{\tau_i}\int\frac{d^3p_i}{(2\pi)^3}\right] n(\mathbf{p}_1)n(\mathbf{p}_2)\bar{n}(\mathbf{p}_3)\bar{n}(\mathbf{p}_4) \times \frac{\langle 12|A_{12}V^{\rm NN}_{\rm LO}|34\rangle\langle 34|A_{12}V^{\rm NN}_{\rm LO}|12\rangle}{\varepsilon_{\mathbf{p}_1}+\varepsilon_{\mathbf{p}_2}-\varepsilon_{\mathbf{p}_3}-\varepsilon_{\mathbf{p}_4}} \times (2\pi)^3\delta^3(\mathbf{p}_1+\mathbf{p}_2-\mathbf{p}_3-\mathbf{p}_4)\,, \tag{33}$$

where

$$\bar{n}(\mathbf{p}_i) \equiv \Theta(|\mathbf{p}_i| - k_{\rm F})\,, \tag{34a}$$

and

$$\varepsilon_{\mathbf{p}_i} = \frac{\hbar^2 p_i^2}{2m}\,. \tag{34b}$$

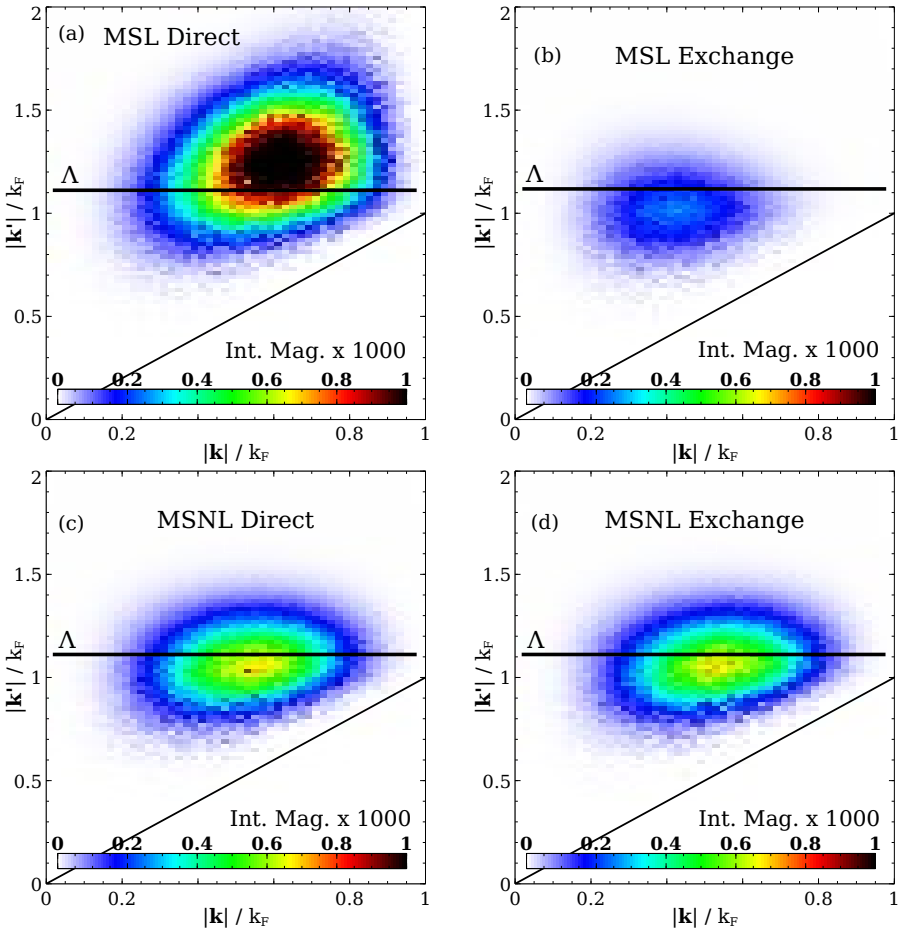

FIG. 11. (color online) Momentum histograms for the integrand magnitude I_2 in (37) at $k_{\rm F} = 1.8$ fm^{-1}, $n = 2$, and $\Lambda_{\rm NN} = 2.0$ fm^{-1}. The integrand magnitude I_2 is also scaled by a factor of 1000. The y-axis gives the particle relative momentum while the x-axis gives the hole relative momentum. Colors indicate the integrand magnitude for a particular k, k' pair. The horizontal black line indicates the cutoff $\Lambda_{\rm NN}$ while the sloping black line separates out the inaccessible region due to Pauli blocking.

For simplicity we use a free spectrum, but we do not expect a different choice to change our discussion. It is also useful to define a new relative momentum,

$$\mathbf{k}' = \frac{\mathbf{p}_3 - \mathbf{p}_4}{2} \,, \tag{35}$$

where $\mathbf{p}_3, \mathbf{p}_4$ correspond to single-particle momenta with magnitudes above the Fermi momentum $k_{\rm F}$.

The momentum transfer for a particular matrix element is defined differently depending on which part of the antisymmetrizer A_{12} acts in the matrix element:

$$\begin{aligned} 1 \implies \langle 12|V|34\rangle : &\qquad \mathbf{q} = \mathbf{p}_1 - \mathbf{p}_3 = \mathbf{k} - \mathbf{k}' \,, \\ P_{12} \implies \langle 21|V|34\rangle : &\qquad \mathbf{q}' = \mathbf{p}_1 - \mathbf{p}_4 = \mathbf{k} + \mathbf{k}' \,. \end{aligned} \tag{36}$$

using the relative momenta definitions in (2) and (35). As such, the second-order direct term will have only $\mathbf{q}$ (or $\mathbf{q}'$) dependence while the exchange term will have both $\mathbf{q}$ and $\mathbf{q}'$ dependence due to the different particle order in the two matrix elements. Both $\mathbf{k}$ and $\mathbf{k}'$ are independent momenta implying that it is not generally possible for both $\mathbf{q}$ and $\mathbf{q}'$ to simultaneously have small magnitudes. Therefore, we expect that local regulators, which act to cut off large momentum transfers, will have suppressed energies (and phase spaces) for exchange terms relative to the direct terms.

The second-order energy values for the C_S–C_S topology and the OPE–OPE topology are given in Fig. 10. (Diagrams with mixed vertices such as C_S–OPE will mix regulator effects; we do not consider them here.) The C_T–C_T term has similar behavior to the C_S–C_S term. In contrast to NN HF energy values in Fig. 4, here the contact CSL regulator in Fig. 10(a) and (b) deviates from the MSL scheme at large $k_{\rm F}$. We attribute this to the oscillating functional form of the CSL regulator in Fig. 5(a); the particle states at large $k_{\rm F}$ probe the 'ringing' of the CSL contact regulator function at large $|\mathbf{q}|$. We also note the large scheme dependence seen in the second-order OPE–OPE energy values, especially with respect to the coordinate space regulators.

Having established the utility of the phase space his-

tograms for Hartree-Fock, we use them as diagnostics at second-order to study where the action of the regulator becomes important for the MSL and MSNL schemes. Representative examples are given in Fig. 11. Because the choice of scheme dominates the phase space distribution, for simplicity, we consider the integrand magnitude weighted only by the regulator functions (cf. with (31) at NN HF),

$$I_2 = |f_{\rm reg}|\; n(\mathbf{P}/2+\mathbf{k})\; n(\mathbf{P}/2-\mathbf{k}) \\ \bar{n}(\mathbf{P}/2+\mathbf{k})\; \bar{n}(\mathbf{P}/2-\mathbf{k})\;. \qquad (37)$$

Weighting by the more complicated full energy integrand does not alter the qualitative features of the histograms (see supplemental material and discussion below).

As in NN HF, single-particle momenta $\mathbf{p}_1, \mathbf{p}_2, \mathbf{p}_3, \mathbf{p}_4$ are randomly generated (subject to the momentum conservation constraint) and the corresponding energy integrand I_2 is calculated. The resulting magnitude is then binned in the histogram. The plots are now two-dimensional, with color serving as a third degree of freedom to indicate the integrand magnitude I_2. Hole and particle relative momentum are plotted on the x- and y-axis respectively, both normalized with respect to $k_{\rm F}$. After all momenta are generated, the plots are then normalized by the total number of k', k pairs generated. Additionally, a black horizontal line indicates the position of the cutoff and the sloping black line near the bottom of the plot separates out the inaccessible region due to Pauli blocking.

A key distinction from NN HF for these second-order phase space plots is that the unregulated k' can range up to arbitrarily high momenta. Thus, while the HF plots in the previous section display a universal profile, the unregulated second-order phase space is infinite in extent and all regulated representations are *inherently* scheme and scale dependent. However, we do expect regulator dependencies to be less important in the lower density limit (see supplemental material).

As the density is raised and $k_{\rm F}$ starts to approach $\Lambda_{\rm NN}$, scheme artifacts will become more apparent. For $k_{\rm F} = 1.8$ fm^{-1} and $\Lambda_{\rm NN} = 2.0$ fm^{-1}, we plot the second-order histograms in Fig. 11 for the direct/exchange terms in the MSL and MSNL schemes.

Looking first at the MSNL histograms in Fig. 11(c) and (d), we see that the distributions of the direct and exchange terms are equivalent. This reflects the permutation symmetry of the nonlocal regulator in (6); direct and exchange terms are cut off in equivalent ways. We also note that the center of the MSNL distribution is at $k \approx 0.55\, k_{\rm F}$. This is similar to the center of the distribution at NN HF (cf. Fig. 7) and at lower densities (see supplemental material). This implies that as the density is raised, the phase space for the MSNL terms are primarily cut off at large k'.

Different behavior is seen for the MSL scheme in Fig. 11(a) and (b). The phase space for the exchange term is suppressed compared to the phase space for the direct term as anticipated above. The exchange term's phase space comes primarily from regions below the cutoff and is much more constrained in magnitude. In contrast, a substantial portion of the direct term's phase space comes from relative momenta k' which are above the cutoff $\Lambda_{\rm NN}$. Furthermore, it is seen in each case that the central profile of the phase space is shifted away from $k \approx 0.55\, k_{\rm F}$. In the direct term, the center is shifted towards large k,k' reflecting the potential cancellation between $\mathbf{k}$ and $\mathbf{k}'$. In the exchange term, the center is shifted towards small k,k'.

We make equivalent plots of the full integrand magnitude for the C_S–C_S and OPE–OPE histograms in the supplemental at $k_{\rm F} = 1.8$ fm^{-1}. These do not display any qualitative differences compared to Fig. 11. This again emphasizes that the regulators are primarily determining the phase space distribution.

We do not address the large scheme dependence seen for the second-order OPE–OPE energy values between the coordinate space regulators. Our histogram approach is not easily adapted to the use of the long-range coordinate space regulator functions at second-order and cannot offer intuition about which parts of the phase space are most relevant.

C. 3N Forces at HF

For a 3-body interaction, the HF energy per particle in terms of the single-particle momenta is given by

$$\frac{E^{\rm 3N}_{\rm HF}}{N} = \frac{1}{6\rho} \sum_{\sigma_1\sigma_2\sigma_3} \sum_{\tau_1\tau_2\tau_3} \int \frac{d^3p_1}{(2\pi)^3} \int \frac{d^3p_2}{(2\pi)^3} \int \frac{d^3p_3}{(2\pi)^3} \\ n(\mathbf{p}_1) n(\mathbf{p}_2) n(\mathbf{p}_3) \langle 123| A_{123} V^{\rm 3N}_{\rm N^2LO} |123\rangle\;, \quad (38)$$

where $V^{\rm 3N}_{\rm N^2LO}$ includes a regularization scheme. The antisymmetrizer in (17) leads to three different classes of terms depending on the number of exchange operators P_{ij}: one term with no exchange operators, three terms with a single exchange operator, and two terms with two exchange operators. These components are respectively dubbed the direct, single-exchange, and double-exchange terms. Note that in this decomposition, single-exchange and double-exchange by our convention refer to *all* the terms with the associated exchange operators (e.g., single-exchange energies include contributions from P_{12}, P_{13}, and P_{23}). Evaluating these different components with the MSNL regulator in (18) and the MSL regulator in (22) give the energies in Fig. 12 for the contact c_E term. The MSL scheme is equivalent to no regulator for the direct term while single-exchange and double-exchange terms are increasingly suppressed. The MSNL scheme has a similar relative effect on all contributions with respect to unregulated HF. Trends for the finite range c_i, c_D pieces are similar (see supplemental material). For both the MSNL and MSL schemes, the c_E term dominates the energy per particle for natural choice of LECs.

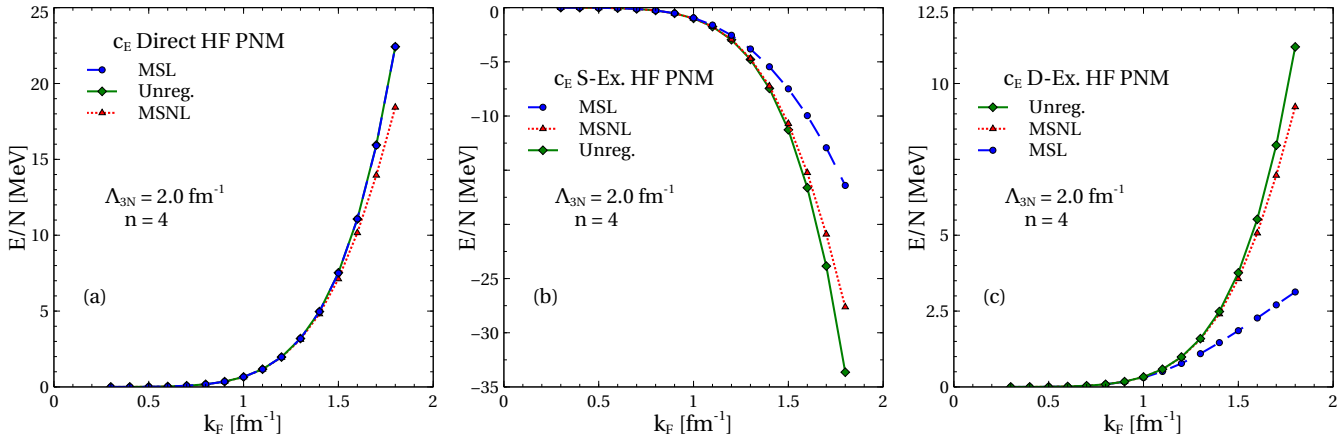

FIG. 12. Plots (a), (b), and (c) show the energy per particle of the c_E term for the direct, single-exchange, and double-exchange topologies respectively in neutron matter with $\Lambda_{3N} = 2.0$ fm^{-1} and $n = 4$.

As before, we analyze momentum histograms to describe the 3N HF phase space. Single-particle momenta $\mathbf{p}_1, \mathbf{p}_2, \mathbf{p}_3$ are randomly generated using Monte Carlo sampling and the 3N HF integrand magnitude,

$$I_3 = |f_{\rm reg}|\, k^2\, j^2\, P^2\, n(\mathbf{P}/3 - \mathbf{j}/2 - \mathbf{k}) \times n(\mathbf{P}/3 - \mathbf{j}/2 + \mathbf{k})\, n(\mathbf{P}/3 + \mathbf{j})\,, \qquad (39)$$

is then calculated for the Jacobi momenta $\mathbf{k}$,$\mathbf{j}$ defined in (20). The integrand magnitude is then binned in a histogram with the moduli of the associated Jacobi momenta, normalized by $k_{\rm F}$, plotted on the y- and x-axes. The sampling process is then repeated and the final distribution is normalized by the total number of Monte Carlo iterations. As in Sec. III B, the resulting histograms are two-dimensional with color intensity denoting integrand magnitudes. Note that in (39) we do not weight the distribution by the different interactions c_i, c_D, c_E. Such weighting is superfluous for our purposes as all the weightings generate similar plots (see supplemental material). As all the momenta in HF are on-shell, the phase space here is unambiguously well-defined, regardless of the cutoff or regulator. As in NN HF, unregulated 3N HF serves as a touchstone to assess scale/scheme dependence via deviations from the unregulated result.

In Fig. 13 we plot representative examples of the full 3N HF phase space for the MSL and MSNL[6] scheme. The color shows the integrand magnitude I_3 for the given regularization scheme while the contour lines indicate the same distribution with no regulator attached to the potential ($f_{\rm reg} \equiv 1$). As at NN second-order, the distribution of points in the weighted phase space is primarily determined by the choice of regulator function.

We make a few general comments:

- The hierarchy in energy values matches the volumes of the different phase spaces i.e., MSL direct > MSNL > MSL single-exchange > MSL double-exchange.
- The MSL direct term is unaltered as the direct diagram has $\mathbf{q}_i = 0$ for all momentum transfers.
- The central profile of the MSNL term is slightly shifted towards smaller k. This reflects the regulator cutting into the hole phase space with exponential suppression of large k, j. Note that the factor of $\frac{3}{4}$ in (19) means that large k will cause more suppression compared to large j.
- The center of the MSL single-exchange histogram is shifted towards small j and k. It also has an asymmetric shape extending out to large $|\mathbf{k}|/\,k_{\rm F}$. This results from the different parts of the 3N interaction not being regulated identically for the different single-exchange components.
- The MSL double-exchange histogram is also shifted to small j and k but to a larger extent than the MSL single-exchange term. As in the single-exchange case, asymmetric features originate from the different momentum transfer possibilities for the two different double-exchange components.

D. 3N Forces at Second-Order

For MBPT at finite density, there exist two types of diagrams resulting from 3-body forces at second-order [39, 53, 54]. These can be found by normal-ordering the free-space second-quantized 3-body operators with respect to a finite density reference state.[7] The first

[6] We only plot the direct term for the MSNL scheme in Fig. 13(a) as the single-exchange and double-exchange terms have the same distribution of points with rescaled magnitudes.

[7] We do not consider the second-order diagram with normal-ordered one-body interactions from the 3-body force because the

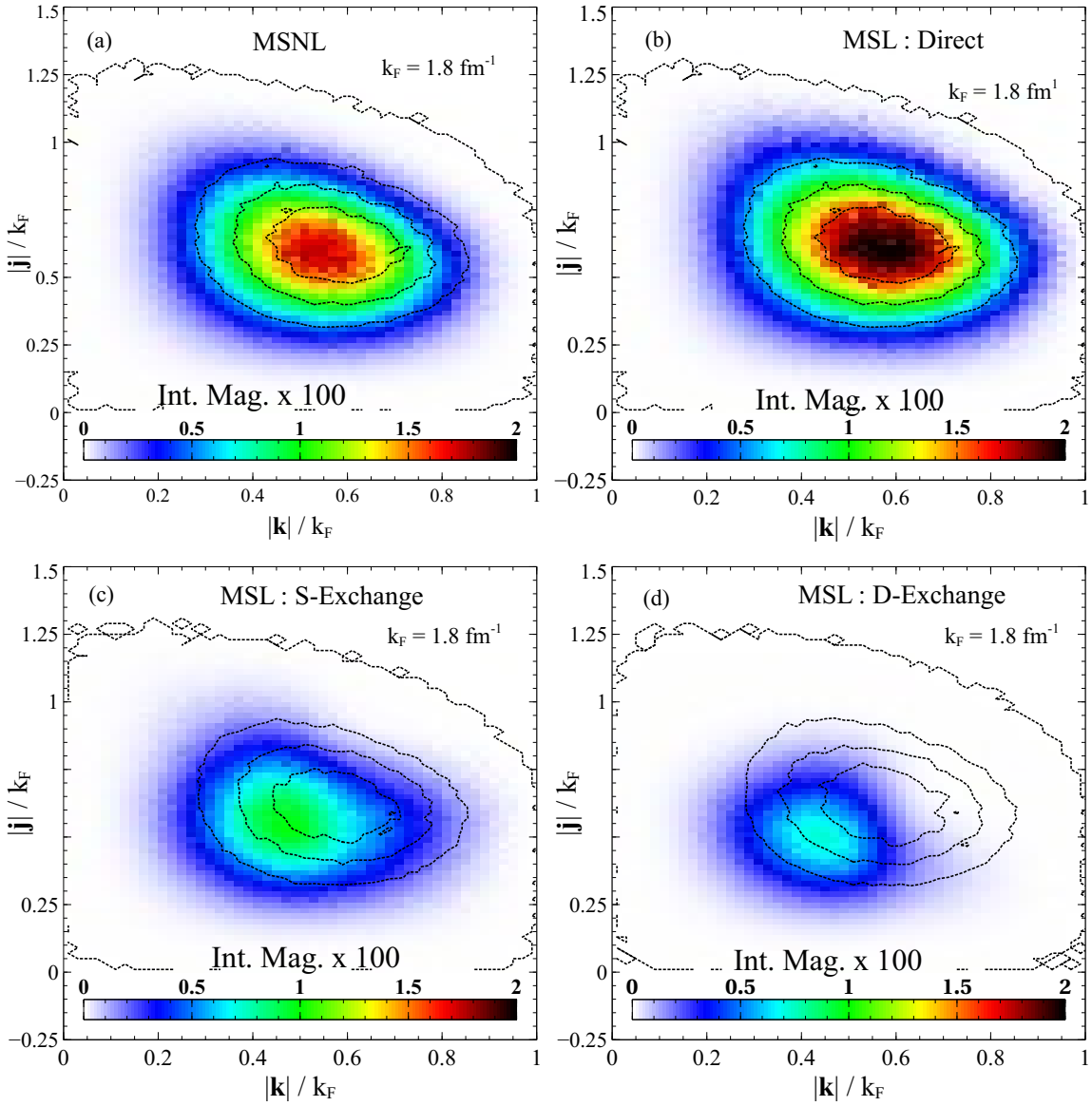

FIG. 13. (color online) Momentum histogram representing the 3N HF phase space for $k_{\rm F} = 1.8$ fm^{-1}, $\Lambda_{\rm 3N} = 2.0$ fm^{-1}, and $n = 4$. The integrand magnitude I_3 in (39) is plotted in color for a given j, k pair normalized by $k_{\rm F}$. The integrand magnitude I_3 is also scaled by a factor of 100. Plot (a) shows the MSNL phase space for the direct term while (b), (c), and (d) show the MSL direct, single-exchange, and double-exchange spaces respectively. The other MSNL terms have an equivalent distribution as the MSNL direct term absent magnitude rescaling. The contour lines indicate the same histogram calculation but with no regulator ($f_{\rm reg} \equiv 1$).

diagram is called normal-ordered or density-dependent (DD), and is found by closing a single-particle line at each 3-body vertex resulting in an effective 2-body interaction. The other diagram, called the residual (RE) diagram, has three particles above and three holes below the Fermi surface and is a true 3-body term. Both diagrams are shown in Fig. 14.

diagram vanishes at zero temperature. The 0-body term is also not considered.

For the DD diagram, we treat the interaction coming from the 3N sector as an effective 2-body force, so our previously defined formula for the second-order NN energy in (33) applies,

$$\frac{E^{\rm 3N}_{\rm DD}}{N} = \frac{1}{4\rho}\left[\prod_{i=1}^{4}\sum_{\sigma_i}\sum_{\tau_i}\int\frac{d^3p_i}{(2\pi)^3}\right] n(\mathbf{p}_1)n(\mathbf{p}_2)\bar{n}(\mathbf{p}_3)\bar{n}(\mathbf{p}_4) \times \frac{\langle 12|A_{12}\overline{V}^{\rm 3N}_{\rm N^2LO}|34\rangle\langle 34|A_{12}\overline{V}^{\rm 3N}_{\rm N^2LO}|12\rangle}{\varepsilon_{\mathbf{p}_1}+\varepsilon_{\mathbf{p}_2}-\varepsilon_{\mathbf{p}_3}-\varepsilon_{\mathbf{p}_4}} \times (2\pi)^3\delta^3(\mathbf{p}_1+\mathbf{p}_2-\mathbf{p}_3-\mathbf{p}_4)\,, \tag{40}$$

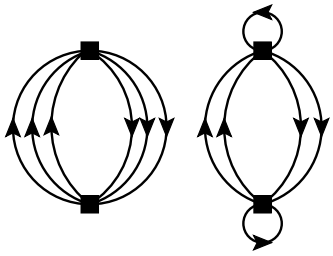

FIG. 14. The residual (left) and normal-ordered (right) second-order diagrams arising from 3-body forces. The NO2B approximation discards the residual term while keeping the normal-ordered digram.

where here we have added an overline to the potential to indicate this normal-ordering prescription with respect to the third particle,

$$\langle 12|\overline{V}^{\rm 3N}_{\rm N^2LO}|45\rangle = \sum_{\sigma_3,\tau_3}\int \frac{d^3p_3}{(2\pi)^3}\; n(\mathbf{p}_3) \times \langle 123|(1-P_{13}-P_{23})V^{\rm 3N}_{\rm N^2LO}|453\rangle \; . \quad (41)$$

For the second-order 3N RE diagram, the energy per particle is given by

$$\frac{E^{\rm 3N}_{\rm RE}}{N} = \frac{1}{36\rho}\Big[\prod_{i=1}^{6}\sum_{\sigma_i}\sum_{\tau_i}\int\frac{d^3p_i}{(2\pi)^3}\Big] \times n(\mathbf{p}_1)n(\mathbf{p}_2)n(\mathbf{p}_3)\bar{n}(\mathbf{p}_4)\bar{n}(\mathbf{p}_5)\bar{n}(\mathbf{p}_6) \times \frac{\langle 123|A_{123}V^{\rm 3N}_{\rm N^2LO}|456\rangle\langle 456|A_{123}V^{\rm 3N}_{\rm N^2LO}|123\rangle}{\varepsilon_{\mathbf{p}_1}+\varepsilon_{\mathbf{p}_2}+\varepsilon_{\mathbf{p}_3}-\varepsilon_{\mathbf{p}_4}-\varepsilon_{\mathbf{p}_5}-\varepsilon_{\mathbf{p}_6}} \times (2\pi)^3\delta^3(\mathbf{p}_1+\mathbf{p}_2+\mathbf{p}_3-\mathbf{p}_4-\mathbf{p}_5-\mathbf{p}_6) \; . \quad (42)$$

Calculations from different many-body methods (e.g. coupled-cluster) have indicated that the DD diagram is larger than the RE diagram [37]. As such, the RE diagram is usually excluded in the normal-ordered 2-body (NO2B) approximation for reasons of computational efficiency. If this approximation is to be well-founded, the contribution of the DD term to the energy density should be much larger than the RE term. That is, the ratio of the contribution of the DD diagram to the RE diagram,

$$R^{3N}_{\rm SO} \equiv \frac{E^{\rm 3N}_{\rm DD}}{E^{\rm 3N}_{\rm RE}} \; , \quad (43)$$

must be much greater than one. The assessment of the NO2B approximation has practical consequences for calculations of finite nuclei and for calculating theoretical error bars. There are also implications for power counting at finite density and the general organization of the many-body problem.

Here we take a simplest first look at the ratio $R^{3N}_{\rm SO}$ using only the c_E 3N contact term. As a benchmark, the ratio $R^{3N}_{\rm SO}$ can be evaluated using dimensional regularization. Assuming the subtraction point is of the same order as $k_{\rm F}$, the ratio is found to be $R^{3N}_{\rm SO} \approx 2$ [55].

For cutoff regularization, we find a significant scale and scheme dependence for $R^{3N}_{\rm SO}$. Evaluating $R^{3N}_{\rm SO}$ for the c_E term in SNM[8] using the MSL and MSNL regulator results in the points in Fig. 15(a). Here the ratio is plotted against the Fermi momentum $k_{\rm F}$ scaled by the cutoff $\Lambda_{\rm 3N}$. Including *all* the N^{2}LO 3N interactions in PNM results in the plot in Fig. 15(b). The qualitative and semi-quantitative features of Fig. 15(a) and (b) are similar, establishing that the inclusion of the finite-range forces and isospin does not appreciably alter this picture.

First, $R^{3N}_{\rm SO}$ in Fig. 15(a) exhibits an obvious scale dependence for both schemes. Staying in a particular scheme at a fixed density, changing the cutoff causes one to move left or right on this plot. At a large cutoff $\Lambda_{\rm 3N}$ compared to $k_{\rm F}$, the particle phase space is not sufficiently cut off and dominates over the hole phase space. The RE diagram has one fewer hole and one extra particle compared to the DD diagram and so consequently, a small $k_{\rm F}/\Lambda_{\rm 3N}$ amplifies the importance of the RE term. Looking at Fig. 15(a) at $k_{\rm F}/\Lambda_{\rm 3N} \approx 0.3$, the diagram ratio $R^{3N}_{\rm SO}$ is $\mathcal{O}(1)$ for the MSNL scheme and already less than 1 for the MSL scheme.

Second, there is a scheme dependence for $R^{3N}_{\rm SO}$; for $k_{\rm F}$ near the cutoff $\Lambda_{\rm 3N}$, the relative importance of the different 3N diagrams in the two schemes differs by almost an order of magnitude. This difference between the two schemes can be understood by examining the effect of the regulator on the different 3N antisymmetric components. As before, we use momentum histograms to highlight the action of the regulator on the phase space.

The relevant integrand magnitudes for the second-order 3N energy, including only Pauli blocking and the regulators, is,

$$I_{4,\rm DD} = |f_{\rm reg}|\; n(\mathbf{p}_5)\; n(\mathbf{p}_6)\; n(\mathbf{P}/2+\mathbf{k}) \times n(\mathbf{P}/2-\mathbf{k})\; \bar{n}(\mathbf{P}/2+\mathbf{k}')\; \bar{n}(\mathbf{P}/2-\mathbf{k}') \; , \quad (44)$$

for the DD term and,

$$I_{4,\rm RE} = |f_{\rm reg}|\; n(\mathbf{P}/3+\mathbf{j})\; \bar{n}(\mathbf{P}/3+\mathbf{j}') \times n(\mathbf{P}/3-\mathbf{j}/2-\mathbf{k})\; n(\mathbf{P}/3-\mathbf{j}/2+\mathbf{k}) \times \bar{n}(\mathbf{P}/3-\mathbf{j}'/2-\mathbf{k}')\; \bar{n}(\mathbf{P}/3-\mathbf{j}'/2+\mathbf{k}') \; , \quad (45)$$

for the RE term. However, now the relevant space is 4-dimensional due to the different momenta moduli which can vary when plotting I_4. We arbitrarily choose to plot I_4 as a function of the two relative momenta moduli k, k' for the DD histogram and the two particle Jacobi momenta moduli k', j' for the RE histogram to better illustrate the effect of the regulator. The histograms for the different antisymmetric components of the DD term are plotted in Fig. 16 for the MSNL and MSL schemes. As can be seen, the distribution is similar to the 2nd order

[8] The c_E term vanishes in PNM for the MSNL scheme so here we switch to using SNM.

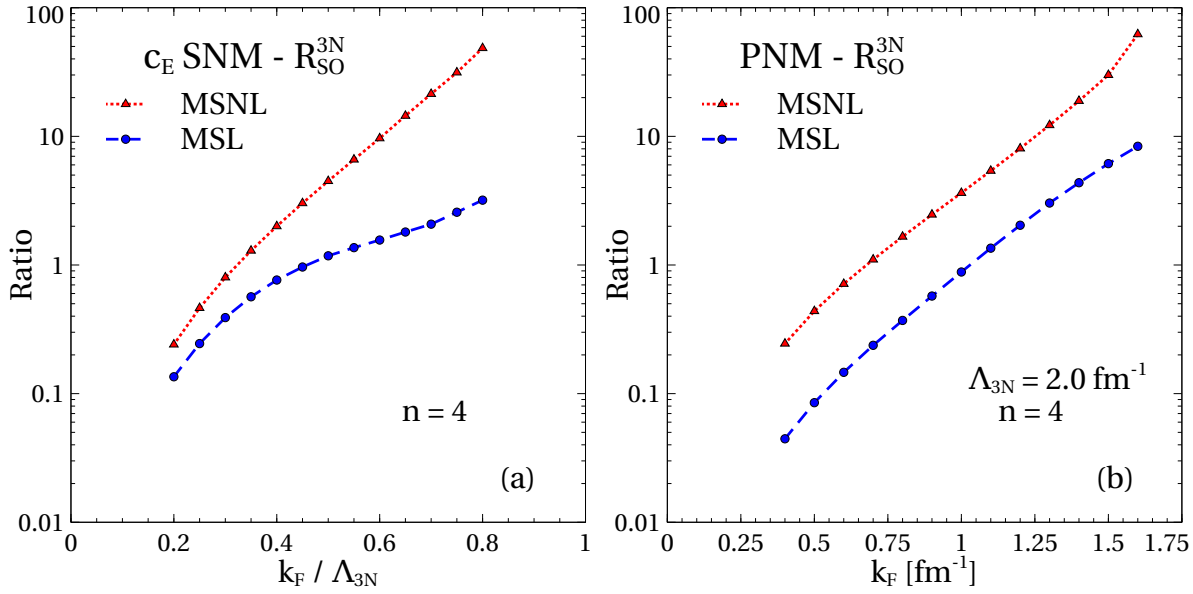

FIG. 15. Plot (a) shows the ratio $R^{3N}_{\rm SO}$ in (43) for the 3N contact term evaluated in SNM. Plot (b) shows the same ratio $R^{3N}_{\rm SO}$ only now including all 3-body interactions in PNM. The trend in the ratio is very similar to plot (a). Both calculations are done with $\Lambda_{\rm 3N} = 2.0$ fm^{-1} and $n = 4$.

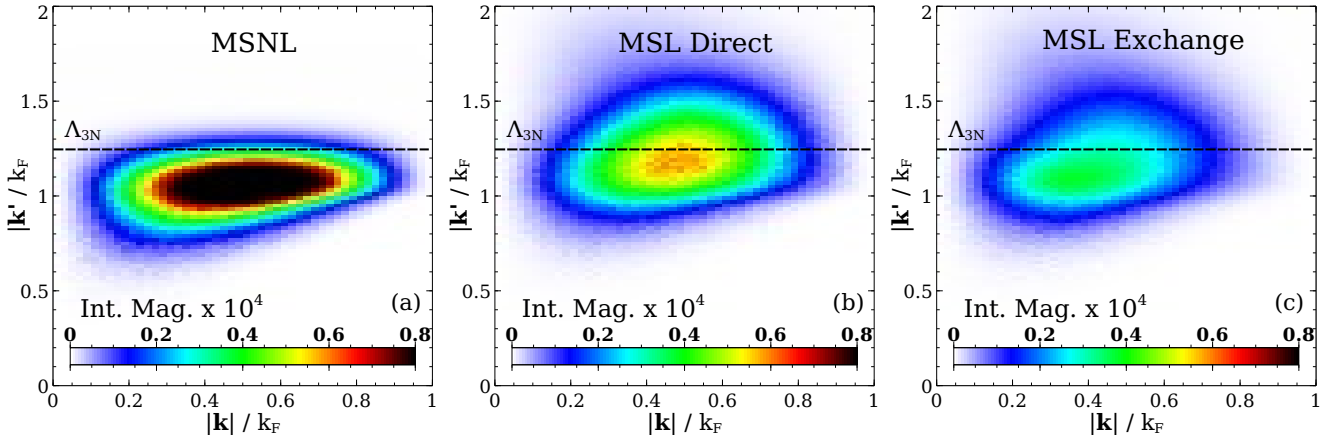

FIG. 16. (color online) Momentum histograms for the 3N second-order normal-ordered term where colors indicate the integrand magnitude $I_{4,\rm DD}$ in (44). The integrand magnitude $I_{4,\rm DD}$ is also scaled by a factor of 10^4. Plots done for the MSNL (a) term and the MSL direct (b) and MSL exchange (c) terms. The direct/exchange MSNL histograms are equivalent due to regulator permutation symmetry. Plotted for $k_{\rm F} = 1.6$ fm^{-1}, $\Lambda_{\rm 3N} = 2.0$ fm^{-1}, $n = 4$. The dashed line indicates the location of the cutoff $\Lambda_{\rm 3N}$.

NN histograms (cf. Fig. 11). The MSNL integrand is cut off at large k' (squeezed from above) while the MSL integrand to some extent includes k' above the cutoff $\Lambda_{\rm 3N}$. This similarity in structure is expected in that the DD term is an effective 2-body interaction. The key difference between the NN second-order and the DD case is the magnitude of the DD MSNL term compared with the DD MSL term. That is, the magnitude of the MSNL term in the DD case is enhanced compared with the MSL term.

Now we examine the residual histograms in Fig. 17. The MSNL scheme in Fig. 17(a) has no k' points above the cutoff and few j' points above $\Lambda_{\rm 3N}$, a difference coming from the factor of 3/4 in the regulator in (19). Due to regulator permutation symmetry, the different MSNL antisymmetric terms (direct, single-exchange, double-exchange) have equivalent distributions. In contrast, the direct MSL term in (b) shows a distinct enhancement coming from small momentum transfers $\mathbf{q}_i$, $\mathbf{q}_j$ in (23). Note also that the range of the direct MSL distribution extends far above the cutoff $\Lambda_{\rm 3N}$. Going to the other MSL antisymmetric pieces in Fig. 17(c) and (d), we see increasing suppression.

Therefore, we can explain the difference in the ratio $R^{3N}_{\rm SO}$ between the two schemes in Fig. 15(a). Relative to

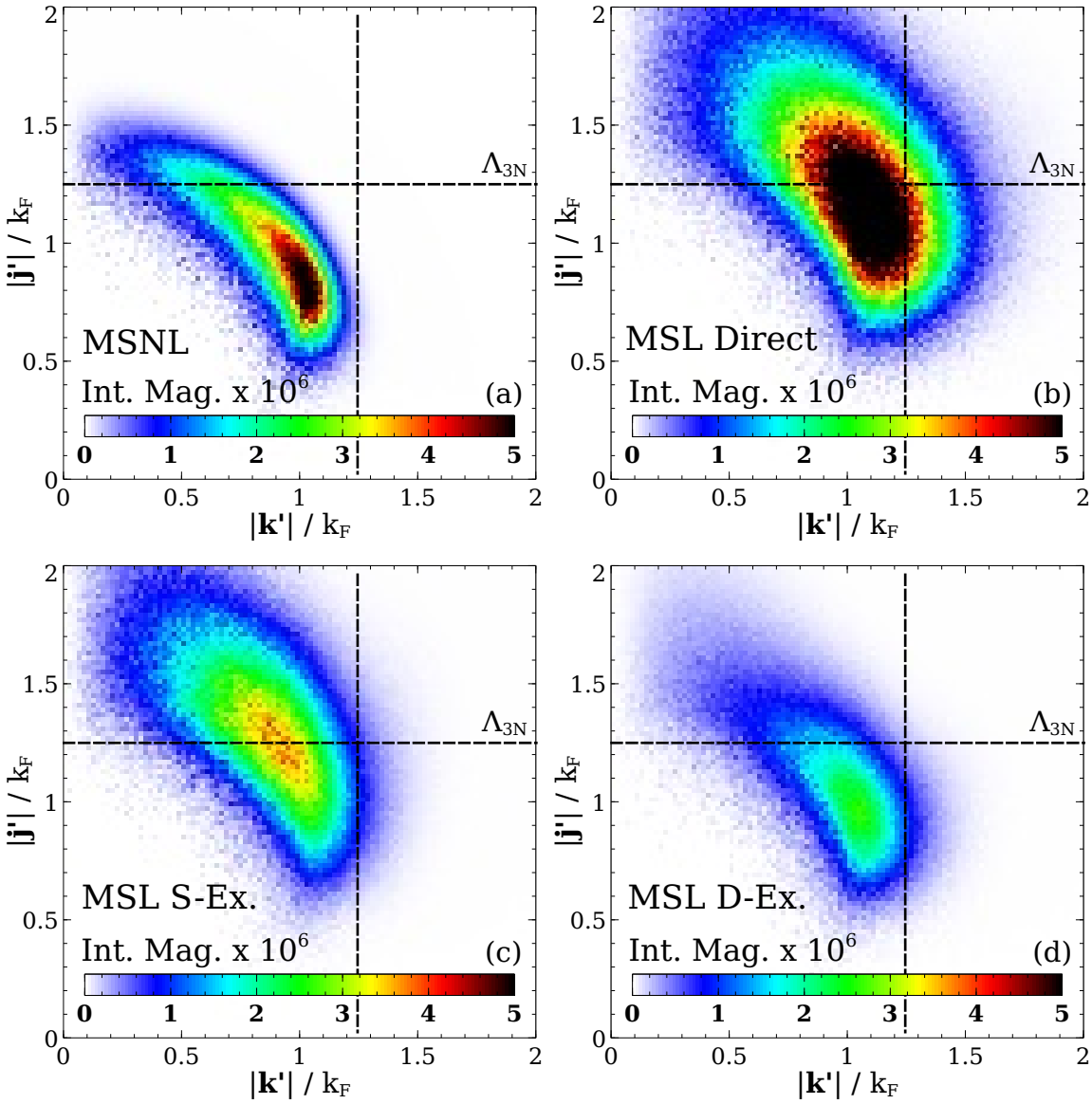

FIG. 17. (color online) Momentum histograms for the 3N second-order residual term where colors indicate the integrand magnitude $I_{4,\mathrm{RE}}$ in (45). The integrand magnitude $I_{4,\mathrm{RE}}$ is also scaled by a factor of 10^6. Plots done for the MSNL (a) term and the MSL direct (b), single-exchange (c), and double-exchange (d) terms. The different MSNL antisymmetric histograms are equivalent due to regulator permutation symmetry. Plotted for $k_{\mathrm{F}} = 1.6$ fm^{-1}, $\Lambda_{3\mathrm{N}} = 2.0$ fm^{-1}, $n = 4$. The dashed lines indicate the location of the cutoff $\Lambda_{3\mathrm{N}}$.

the MSNL scheme, the suppression of the DD MSL terms and the enhancement of the direct RE MSL term doubly act to keep R_{SO}^{3N} small for the MSL scheme.

E. Fierz Rearrangements

When constructing the pure 3-body contact coming in at N^{2}LO, there are six different possible spin-isospin structures which satisfy all the relevant symmetries of the low-energy theory [45],

$$V_{\mathrm{con}}^{\mathrm{3NF}} = \sum_{i\neq j\neq k} \big[\beta_1 + \beta_2 \boldsymbol{\sigma}_i\cdot\boldsymbol{\sigma}_j + \beta_3 \boldsymbol{\tau}_i\cdot\boldsymbol{\tau}_j + \beta_4 \left(\boldsymbol{\sigma}_i\cdot\boldsymbol{\sigma}_j\right)\left(\boldsymbol{\tau}_i\cdot\boldsymbol{\tau}_j\right) + \beta_5 \left(\boldsymbol{\sigma}_i\cdot\boldsymbol{\sigma}_j\right)\left(\boldsymbol{\tau}_j\cdot\boldsymbol{\tau}_k\right) + \beta_6 \left(\left[\boldsymbol{\sigma}_i\times\boldsymbol{\sigma}_j\right]\cdot\boldsymbol{\sigma}_k\right)\left(\left[\boldsymbol{\tau}_i\times\boldsymbol{\tau}_j\right]\cdot\boldsymbol{\tau}_k\right)\big] . \quad (46)$$

Using Fierz rearrangements it can be shown that, up to numerical prefactors, only one of the above operator structures is linearly independent. As such, it is only necessary to include one of the six operator structures in χEFT when fitting LECs and doing calculations. The typical choice made in current applications is to use

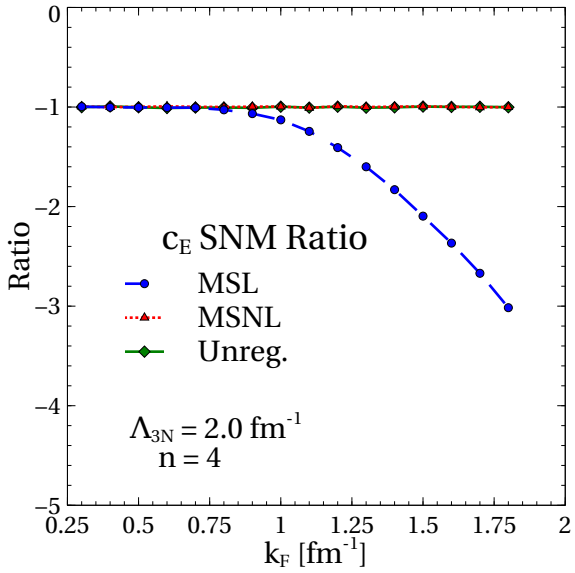

FIG. 18. The ratio for the 3N HF energy in (47) of the c_E contact term in SNM calculated with two different operator structures. The numerator (denominator) was calculated with the operator corresponding to $\beta_1(\beta_3)$ in (46).

$\boldsymbol{\tau}_i \cdot \boldsymbol{\tau}_j$ corresponding to β_3 in (46). However, a complication enters when the regulator is no longer symmetric under individual nucleon permutation e.g., the MSL regulator in (22) [38, 49]. The Fierz relations establishing equivalence between the different operator structures are spoiled when the antisymmetric pieces of the 3N interaction are regulated differently. This ambiguity of the 3N contact operator for local regulators has recently been explored in Ref. [56].

This point can be seen in our perturbative approach to the uniform system. In Fig. 18, we plot a calculation of the ratio of the 3N HF energy for the operator choices corresponding to β_1 and β_3 in (46):

$$E_1^{\rm HF}/E^{\rm HF}_{\boldsymbol{\tau}_i\cdot\boldsymbol{\tau}_j}\ . \tag{47}$$

Using the MSNL regulator, or no regulator at all, the ratio of the two different HF energy calculations in (47) is constant with respect to density. This reflects the pure numerical prefactor between the different operators one gets upon Fierz rearrangement. However, when using the MSL regulator, the ratio between the two calculations is now density-dependent. It is an open question to what extent this Fierz ambiguity is resolved by including three-nucleon contributions at higher orders in the chiral expansion when using regulators that do not respect permutation symmetry.

IV. SUMMARY AND OUTLOOK

Recent progress in nuclear many-body methods has led to increasingly precise ab initio calculations of observables over a growing range of nuclei. This in turn has shifted focus to the input χEFT Hamiltonian in the quest for more accurate calculations and a systematic understanding of theoretical uncertainties. A major source of variation among Hamiltonians currently considered stems from the regularization scheme chosen, because χEFT implemented using Weinberg power counting is not renormalizable order by order. As such there remains residual cutoff dependences in the theory to all orders and regulator artifacts, which are scheme dependencies that remain after implicit renormalization, are inevitable.

In this work, we characterized the impact of various NN and 3N regulator choices by analyzing perturbative energy calculations in the uniform system at Hartree-Fock and second-order using the leading NN/3N chiral interactions. This allows us to test both long-range and contact potentials, and both the on-shell and off-shell parts.

We find significant scale and scheme dependence for perturbative energy calculations at finite density using chiral forces and the scheme choices outlined in Table I. In particular, we have identified characteristic regulator artifacts resulting from the differing regulator functional forms. To uncover the origins of the differing behavior of energy calculations, we adopted an approach based on analyzing the phase space available at each order in MBPT using a Monte Carlo sampling of momenta. In all cases, it is this phase space that serves as a guidepost to the effect of different schemes. The momentum histograms in section III are used to show:

- the extent and shape of the phase space;
- the connection between the size of the phase space and the total computed energy;
- which parts of the phase space are suppressed by the regulator;

- how the regulator cuts off the phase space.

We anticipate that this histogram diagnostic will have wider applications, such as in assessing finite-density power counting or in guiding the implementation of long-range chiral forces in nuclear density functionals via the density matrix expansion [8, 57–61].

Here we summarize some of our observations from Sec. III about scale and scheme dependencies:

- In special cases where the regulators can be directly related to one another, scheme dependence translates simply to a different effective cutoff. For example, the MSNL (6) and MSL (8) schemes at NN HF can be put into equivalence (32) due to the relation between momentum transfer and relative momentum. Likewise, the MSL and CSL contact (12) regulator for $n = 1$ allows $\Lambda_{\rm NN}$ and R_0 to be directly related (27) to each other. But in general regulators cannot be put into a direct correspondence.

- Coordinate space regulators (usually) lead to oscillatory behavior when Fourier transformed (see Fig. 5). In contrast to the smooth cutoff behavior of the momentum space regulators, this manifests as zero points in the interaction phase space, see CSL/EKM in Fig. 7(c).

- Our primary analysis tool are phase space histograms, which are used to understand the effect of the regulator at different orders of MBPT. The analytic form of the energy integrand in MBPT is only easily found at NN HF. The expression in (28) and the plot in Fig. 6 shows this analytic form plotted for the HF exchange term with the $n \to \infty$ limit for the MSNL and MSL schemes as given in (29) and (30). Our histogram approach reproduces this picture in the sharp regulator limit as demonstrated in Fig. 8. Likewise, examining the NN HF energy per particle calculations in Fig. 4, we find an exact matching in the energy hierarchy to the phase space volume for the histograms in Fig. 7. The same observation can also be made for the MSL and MSNL NN second-order energies (Fig. 10) and histograms (Fig. 11) along with the 3N HF energy (Fig. 12) and histograms (Fig. 13).

- The qualitative scale dependence of all the regulators is similar, with softer cutoffs (i.e., those with smaller $\Lambda_{\rm NN}$, $\Lambda_{\rm 3N}$, and larger R_0) generating larger energy differences at a fixed density. In regions where the Fermi momentum $k_{\rm F}$ is small compared to the cutoff, scheme artifacts are generally small. However, finite range coordinate space regulators (CSL/EKM) have modifications that persist even at small q (Fig. 5) leading to differences at small $k_{\rm F}$ (Fig. 7(c) and Fig. 9). Note that to highlight scheme effects, in this paper we worked at soft cutoffs of $\Lambda_{\rm NN} = 2.0$ fm^{-1}, $R_0 = 1.2$ fm, and $\Lambda_{\rm 3N} = 2.0$ fm^{-1}. Calculations with harder cutoffs present quantitative smaller artifacts but are qualitatively similar (see supplemental material).

- At higher densities, regulators cut into the hole phase space and at second-order (and beyond) the regulators squeeze the particle phase space, making artifacts more apparent. This can be seen in the NN HF histograms of Fig. 7 where scheme differences become larger as $k_{\rm F}$ increases. Likewise in the NN second-order histograms, large differences exist at large $k_{\rm F}$ between different schemes (Fig. 11 and Figs. 21, 22). The corresponding effects are seen for 3N HF (Fig. 13) and at 3N second-order (Figs. 16, 17).

- The behavior of the regulator under permutation symmetry, the interchanging of nucleon labels i, j due to the exchange operator P_{ij}, affects how the different parts of the potential are affected i.e., direct vs. exchange. Stark differences in behavior can occur when the regulator does not respect permutation symmetry. Certain regulator schemes respect (MSNL) or do not respect (MSL) permutation symmetry. At the NN HF level, the phase space histograms can clearly demonstrate this fact (cf. Fig. 7(a) and (b) at $k_{\rm F} = 1.8$ fm^{-1} for MSL and MSNL). The direct/exchange components in the MSL scheme are very different but they are identical in the MSNL scheme. This manifests at second-order as well, as can be seen in comparing Fig. 11(a) and (b) for the MSL scheme along with (c) and (d) for the MSNL scheme. 3-body contributions at HF and second-order also display these differences between antisymmetric components in different schemes in Figs. 13, 16, and 17.

- Additionally, how regulators behave under permutation symmetry can affect Fierz rearrangements between operator structures. In particular, when constructing the N^{2}LO 3N contact term, six different possible operator structures exist which respect the relevant symmetries of χEFT, see (46). However, upon Fierz rearrangement, only one operator is shown to be linearly independent. As a result, different operator structures can be related to one another and differ only by a pure numerical prefactor. However, these rearrangements depend on relations between different antisymmetric components of the operators. For regulators which do not respect permutation symmetry (e.g., the MSL scheme), these Fierz rearrangements are no longer automatic. In Sec. III E, we show that the Fierz relation is spoiled for two operator choices in a 3N HF energy calculation using the MSL scheme (see Fig. 18).

- Approximations of many-body perturbation theory (MBPT) also exhibit scheme and scale dependence. For 3N forces, a common technique is to

normal-order the free-space second-quantized operators with respect to a finite density ground state. At second-order in MBPT, this results in an effective 2-body term (called the normal-ordered term) and a remaining 3-body piece (called the residual term). The residual term is a true 3-body term and is computationally expensive to calculate. In the NO2B approximation, the residual term is discarded and the computationally simple normal-ordered term is retained. Such an approximation is only valid if the contribution of the normal-ordered term to the energy is greater than the residual i.e., if the ratio of the former to latter is greater than one.

In Sec. III D, we demonstrated that the ratio of the normal-ordered term to the residual term has a distinct scheme and scale dependence. The scale dependence comes from changing the extent and importance of the hole/particle phase space as the cutoff is changed. As the cutoff is raised, the particle phase space increases and the residual term dominates. We use our momentum histograms to understand the scheme dependence for the MSNL and MSL schemes. In the MSL scheme, the direct residual term is enhanced due to small momentum transfers $\mathbf{q}_{i,j}$ (Fig. 17(b)) while the normal-ordered terms are suppressed compared to the MSNL scheme (Fig. 16). This residual term enhancement and normal-ordered term suppression in the MSL scheme results in very different ratios for local and nonlocal schemes, as seen in Fig. 15.

- While we have emphasized the dominant role of the phase space, there are also quantitative differences in calculations due to the role of the interaction and how it interplays with the chosen scheme. For example, the 3N c_1 term weights states lower in the Fermi sea (see supplemental material and Fig. 27). Consequently, c_1 scheme dependence and regulator artifacts are less pronounced than compared with c_3, c_D, and c_E.

A critical but open question is the ultimate impact of the regulator artifacts. For example, it has been seen that two-pion exchange regulator artifacts can affect the chiral power counting in uniform matter [62]. However, recent research has indicated that these artifacts are better controlled using certain coordinate-space local regulators (e.g., see Table VII in [33], which illustrates insensitivity to the functional form and cutoff of the regulator). Whether local regulators are the only way to control finite range artifacts, and avoid distorting analytic structures, remains an open question.

If χEFT is to be model independent and follow the chiral power counting, regulator artifacts at one order must be absorbed at higher order consistent with the power counting. But how the regulator dependence is absorbed (if it is) by implicit renormalization is not manifest. Furthermore, a systematic comparison of uncertainties due to truncation of the chiral expansion and truncation in MBPT still needs to be explored.

The significant regulator artifacts observed here and for two-pion exchange motivate exploration of a wider range of functional forms for regulators, such as those commonly used for the functional renormalization group (RG) [63] and nuclear low-momentum RG evolution (e.g., see Ref. [64]). For example, there are regulators with an independent dimensional scale parameter to set the smoothness of the cutoff, instead of relying on a super-Gaussian suppression. This may provide greater control over artifacts. The analysis tools introduced here are being applied to these alternatives in an ongoing investigation.

ACKNOWLEDGEMENTS

We would like to thank Christian Drischler for numerical comparisons and Achim Schwenk for useful discussions. We would also like to thank Joel Lynn, Stefano Gandolfi, Alessandro Lovato, and other colleagues in the NUCLEI collaboration. This work was supported in part by the National Science Foundation under Grant No. PHY-1306250 and Grant No. PHY-1430152 (JINA Center for the Evolution of the Elements), the NUCLEI SciDAC Collaboration under DOE Grant DE-SC0008533 and DOE Grant No. DE-FG02-00ER41132, and by the ERC Grant No. 307986 STRONGINT.

[1] E. Epelbaum, H.-W. Hammer, and U.-G. Meißner, Rev. Mod. Phys. **81**, 1773 (2009).
[2] R. Machleidt and D. Entem, Physics Reports **503**, 1 (2011).
[3] R. Roth, J. Langhammer, A. Calci, S. Binder, and P. Navratil, Phys. Rev. Lett. **107**, 072501 (2011).
[4] R. Roth, S. Binder, K. Vobig, A. Calci, J. Langhammer, *et al.*, Phys. Rev. Lett. **109**, 052501 (2012).
[5] T. A. Lähde, E. Epelbaum, H. Krebs, D. Lee, U.-G. Meißner, and G. Rupak, Phys. Lett. B **732**, 110 (2014).
[6] P. Maris, J. P. Vary, and A. M. Shirokov, Phys. Rev. C **79**, 014308 (2009).
[7] P. Navratil, R. Roth, and S. Quaglioni, Phys. Rev. C **82**, 034609 (2010).
[8] S. Bogner, R. Furnstahl, H. Hergert, M. Kortelainen, P. Maris, *et al.*, Phys. Rev. C **84**, 044306 (2011).
[9] G. Hagen, T. Papenbrock, D. J. Dean, and M. Hjorth-Jensen, Phys. Rev. C **82**, 034330 (2010).
[10] H. Hergert, S. Binder, A. Calci, J. Langhammer, and R. Roth, Phys. Rev. Lett. **110**, 242501 (2013).

[11] H. Hergert, S. Bogner, T. Morris, A. Schwenk, and K. Tsukiyama, Physics Reports **621**, 165 (2016).
[12] A. Carbone, A. Polls, and A. Rios, Phys. Rev. C **88**, 044302 (2013).
[13] S. Fiorilla, N. Kaiser, and W. Weise, Nucl. Phys. A **880**, 65 (2012).
[14] K. Hebeler, S. K. Bogner, R. J. Furnstahl, A. Nogga, and A. Schwenk, Phys. Rev. C **83**, 031301 (2011).
[15] G. Hagen, T. Papenbrock, A. Ekström, K. A. Wendt, G. Baardsen, S. Gandolfi, M. Hjorth-Jensen, and C. J. Horowitz, Phys. Rev. C **89**, 014319 (2014).
[16] I. Tews, T. Krüger, K. Hebeler, and A. Schwenk, Phys. Rev. Lett. **110**, 032504 (2013).
[17] G. Hagen, T. Papenbrock, M. Hjorth-Jensen, and D. J. Dean, Rept. Prog. Phys. **77**, 096302 (2014).
[18] J. W. Holt, M. Rho, and W. Weise, (2014), arXiv:1411.6681 [nucl-th].
[19] A. Ekström, G. R. Jansen, K. A. Wendt, G. Hagen, T. Papenbrock, B. D. Carlsson, C. Forssén, M. Hjorth-Jensen, P. Navrátil, and W. Nazarewicz, Phys. Rev. C **91**, 051301 (2015).
[20] K. Hebeler, J. Holt, J. Menéndez, and A. Schwenk, Annual Review of Nuclear and Particle Science **65**, 457 (2015).
[21] J. Simonis, K. Hebeler, J. D. Holt, J. Menéndez, and A. Schwenk, Phys. Rev. C **93**, 011302 (2016).
[22] A. Cipollone, C. Barbieri, and P. Navrátil, Phys. Rev. Lett. **111**, 062501 (2013).
[23] B. R. Barrett, P. Navratil, and J. P. Vary, Prog. Part. Nucl. Phys. **69**, 131 (2013).
[24] G. Hagen, A. Ekstrom, C. Forssen, G. R. Jansen, W. Nazarewicz, T. Papenbrock, K. A. Wendt, S. Bacca, N. Barnea, B. Carlsson, C. Drischler, K. Hebeler, M. Hjorth-Jensen, M. Miorelli, G. Orlandini, A. Schwenk, and J. Simonis, Nat Phys **12**, 186 (2016).
[25] S. Weinberg, Phys. Lett. B **251**, 288 (1990).
[26] S. Weinberg, Nucl. Phys. B **363**, 3 (1991).
[27] U. van Kolck, Phys. Rev. C **49**, 2932 (1994).
[28] D. B. Kaplan, M. J. Savage, and M. B. Wise, Nucl. Phys. B **478**, 629 (1996).
[29] N. Klein, D. Lee, W. Liu, and U.-G. Meißner, Physics Letters B **747**, 511 (2015).
[30] G. Lepage, (1997), nucl-th/9706029.
[31] A. Nogga, R. G. E. Timmermans, and U. van Kolck, Phys. Rev. C **72**, 054006 (2005).
[32] E. Epelbaum, W. Glockle, and U.-G. Meissner, Nucl. Phys. A **747**, 362 (2005).
[33] E. Epelbaum, H. Krebs, and U. G. Meißner, Eur. Phys. J. A **51**, 53 (2015).
[34] S. C. Pieper and R. B. Wiringa, Ann. Rev. Nucl. Part. Sci. **51**, 53 (2001).
[35] S. C. Pieper, Nucl. Phys. A **751**, 516 (2005).
[36] A. Gezerlis, I. Tews, E. Epelbaum, S. Gandolfi, K. Hebeler, *et al.*, Phys. Rev. Lett. **111**, 032501 (2013).
[37] G. Hagen, T. Papenbrock, D. J. Dean, A. Schwenk, A. Nogga, M. Włoch, and P. Piecuch, Phys. Rev. C **76**, 034302 (2007).
[38] I. Tews, S. Gandolfi, A. Gezerlis, and A. Schwenk, Phys. Rev. C **93**, 024305 (2016).
[39] K. Hebeler and A. Schwenk, Phys. Rev. C **82**, 014314 (2010).
[40] D. R. Entem and R. Machleidt, Phys. Rev. C **68**, 041001 (2003).
[41] T. Krüger, I. Tews, K. Hebeler, and A. Schwenk, Phys. Rev. C **88**, 025802 (2013).
[42] A. Gezerlis, I. Tews, E. Epelbaum, M. Freunek, S. Gandolfi, *et al.*, Phys. Rev. C **90**, 054323 (2014).
[43] E. Epelbaum, H. Krebs, and U.-G. Meißner, Phys. Rev. Lett. **115**, 122301 (2015).
[44] V. G. J. Stoks, R. A. M. Klomp, C. P. F. Terheggen, and J. J. de Swart, Phys. Rev. C **49**, 2950 (1994).
[45] E. Epelbaum, A. Nogga, W. Glöckle, H. Kamada, U.-G. Meißner, and H. Witała, Phys. Rev. C **66**, 064001 (2002).
[46] H.-W. Hammer, A. Nogga, and A. Schwenk, Rev. Mod. Phys. **85**, 197 (2013).
[47] S. K. Bogner, R. J. Furnstahl, A. Nogga, and A. Schwenk, arXiv:0903.3366 [nucl-th].
[48] P. Navratil, Few Body Syst. **41**, 117 (2007).
[49] A. Lovato, O. Benhar, S. Fantoni, and K. E. Schmidt, Phys. Rev. C **85**, 024003 (2012).
[50] S. K. Bogner, A. Schwenk, R. J. Furnstahl, and A. Nogga, Nucl. Phys. A **763**, 59 (2005).
[51] R. J. Furnstahl, J. V. Steele, and N. Tirfessa, Nucl. Phys. A **671**, 396 (2000).
[52] A. L. Fetter and J. D. Walecka, *Quantum Many-Particle Systems* (McGraw–Hill, New York, 1972).
[53] J. W. Holt, N. Kaiser, and W. Weise, Phys. Rev. C **81**, 024002 (2010).
[54] A. Carbone, A. Rios, and A. Polls, Phys. Rev. C **90**, 054322 (2014).
[55] N. Kaiser, Eur. Phys. J. A **48**, 58 (2012).
[56] J. E. Lynn, I. Tews, J. Carlson, S. Gandolfi, A. Gezerlis, K. E. Schmidt, and A. Schwenk, Phys. Rev. Lett. **116**, 062501 (2016).
[57] J. W. Negele and D. Vautherin, Phys. Rev. C **5**, 1472 (1972).
[58] J. W. Negele and D. Vautherin, Phys. Rev. C **11**, 1031 (1975).
[59] B. Gebremariam, S. Bogner, and T. Duguet, Nuclear Physics A **851**, 17 (2011).
[60] M. Stoitsov, M. Kortelainen, S. Bogner, T. Duguet, R. Furnstahl, *et al.*, Phys. Rev. C **82**, 054307 (2010).
[61] S. K. Bogner, R. J. Furnstahl, and L. Platter, Eur. Phys. J. A **39**, 219 (2009).
[62] K. Hebeler, H. Krebs, E. Epelbaum, J. Golak, and R. Skibiński, Phys. Rev. C **91**, 044001 (2015).
[63] J. M. Pawlowski, M. M. Scherer, R. Schmidt, and S. J. Wetzel, (2015), arXiv:1512.03598 [hep-th].
[64] S. K. Bogner, R. J. Furnstahl, S. Ramanan, and A. Schwenk, Nucl. Phys. A **784**, 79 (2007).

Appendix A: NN Energy Values at Harder Cutoffs

In this appendix we show plots for the energy per particle at NN HF using more common cutoffs of $\Lambda_{\rm NN} = 2.5$ fm^{-1} and $R_0 = 0.9$ fm for position space regulators. The antisymmetric terms for the energy per particle for NN HF are given in Fig. 19. These can be compared to the energy calculations at the softer cutoffs $\Lambda_{\rm NN} = 2.0$ fm^{-1}, $R_0 = 1.2$ fm in Fig. 4. Note that energy values between the different schemes are more similar here compared with the $\Lambda_{\rm NN} = 2.0$ fm^{-1} case; i.e., regulator artifacts for $\Lambda_{\rm NN} = 2.5$ fm^{-1} are less pronounced at a given $k_{\rm F}$.

Appendix B: NN Second-Order I_2 Plots

In Sec. III B, the histogram plots are weighted by the phase space I_2 in (37) rather than the full integrand magnitude. The full second-order energy integrand $I_{2,\rm full}$ is given by,

$$\begin{aligned} I_{2,\rm full} &= |f_{\rm reg}| \, \frac{k^2 \; k'^2 \; P^2}{(k'^2/m - k^2/m)} \\ &\times n(\mathbf{P}/2+\mathbf{k}) \; n(\mathbf{P}/2-\mathbf{k}) \; \bar{n}(\mathbf{P}/2+\mathbf{k}') \; \bar{n}(\mathbf{P}/2-\mathbf{k}') \\ &\times \begin{cases} 1, & \text{Contact} \, , \\ \left| \dfrac{q^2 \; S_{12}(\hat{\mathbf{q}}) - m_\pi^2 \boldsymbol{\sigma}_1 \cdot \boldsymbol{\sigma}_2}{q^2 + m_\pi^2} \right|, & \text{OPE} \, , \end{cases} \end{aligned} \tag{B1}$$

where the first (second) term in brackets corresponds to weighting by the contact (OPE) interaction and all spin terms are summed over. In Fig. 20 we plot two examples of this full second-order phase space at a low density $k_{\rm F} = 0.5$ fm^{-1} with a cutoff $\Lambda_{\rm NN} = 2.0$ fm^{-1}. In Fig. 20(a) and (b), we show the MSL direct C_S–C_S term and the MSL direct OPE–OPE term respectively. Here we have only plotted the MSL direct terms because the equivalent MSNL plots are nearly identical (scheme artifacts are small). Likewise, the exchange plots have an equivalent distribution, but with smaller magnitudes.

The circular shapes in the color in Fig. 20 are interpreted as no correlation in the selection of k and k' at lower densities. This can be manifested by rewriting (33) using relative and center-of-mass coordinates.

Looking at Figs. 21 and 22, we see the histogram plots for the C_S–C_S and OPE–OPE terms respectively. The integrand magnitude $I_{2,\rm full}$ of the two terms in (B1) are given by the color intensity for a given k',k pair. Comparing with Fig. 11, it is seen that there is little qualitative difference between plotting just the phase space (I_2) or the full energy integrand ($I_{2,\rm full}$) absent magnitude rescaling. Thus, it is the regularization scheme which primarily drives the distribution of points in the histograms.

Appendix C: Finite Range Interactions at 3N HF

In Sec. III C, only the HF energy per particle for the c_E term was given. Here, we show plots for the energy per particle for the finite range pieces as well. Fig. 23 shows the c_1, c_3, and c_D single-exchange contributions while Fig. 24 shows the double-exchange contributions to the energy per particle. The direct terms for the finite range interactions vanish at HF from tracing over spin-isospin. Comparing with Fig. 12, there is little qualitative difference in the scheme hierarchy for the different interactions (but see App. E).

Appendix D: 3N HF I_3 Plots

Here, we demonstrate that weighting by the finite range interaction c_1 does not qualitatively change the phase space histograms. In Fig. 25, we plot the integrand magnitude I_3 in (39) including a c_1 weighting term from (16) analogously to what is done in (B1) for NN second-order. The integrand magnitude is plotted as a function of the moduli of the Jacobi momenta defined in (20). Comparing to Fig. 13, the two plots are seen to be qualitatively the same.

Appendix E: 3N HF Interaction Terms

In this appendix, we illustrate how different regularization schemes interplay with the form of the different N^{2}LO 3N interactions. As seen in the 3N HF energy per particle plot of Fig. 12, a clear hierarchy is established for the antisymmetric components of the MSNL and MSL schemes (MSL > MSNL for the direct term but MSNL > MSL for the exchange terms). Although, Fig. 12 only shows the c_E term, this hierarchy is generic for the finite range interactions as well. In Fig. 26, we plot the ratio of the energy per particle in PNM for the different schemes,

$$E^{\rm 3N}_{\rm MSNL} \; / \; E^{\rm 3N}_{\rm MSL} \, , \tag{E1}$$

that is the ratio of the HF energy per particle of the MSNL scheme to the MSL scheme. As can be seen, there are two different trends in the above ratio for the exchange terms, one for c_1 and one for c_3, c_D, and c_E.

To see the origin of this difference, we count powers of the momentum transfer in (16b) and (16d) and find one-dimensional variants of the c_1, c_3, c_D interactions in Fig. 27 ignoring spin-isospin,

$$f(q) = \begin{cases} \dfrac{q^2}{(q^2+m_\pi^2)^2} & c_1 \\ \dfrac{q^4}{(q^2+m_\pi^2)^2} & c_3 \\ \dfrac{q^2}{(q^2+m_\pi^2)} & c_D \end{cases} \, . \tag{E2}$$

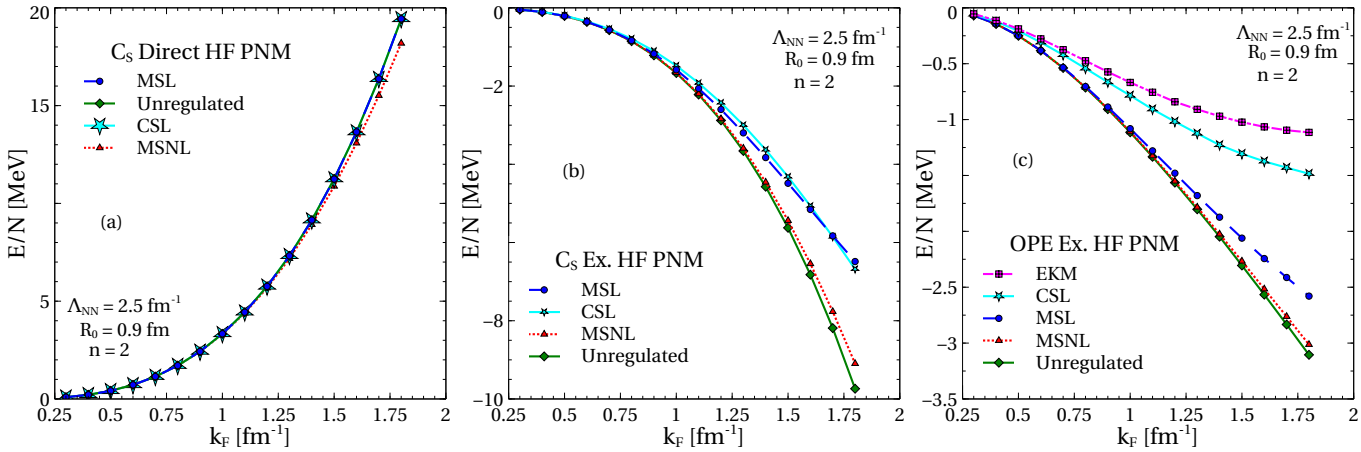

FIG. 19. Neutron matter calculations of the HF energy per particle for the direct (a) and exchange (b) terms for C_S and the OPE exchange term (c) using the regularization schemes in Table I. The C_T calculation has similar behavior to the C_S exchange term. The trends in SNM (not shown) are comparable to those in PNM. The calculations use $C_S = 1.0$ MeV^{-2}, $n = 2$, $\Lambda_{\rm NN} = 2.5$ fm^{-1}, and $R_0 = 0.9$ fm.

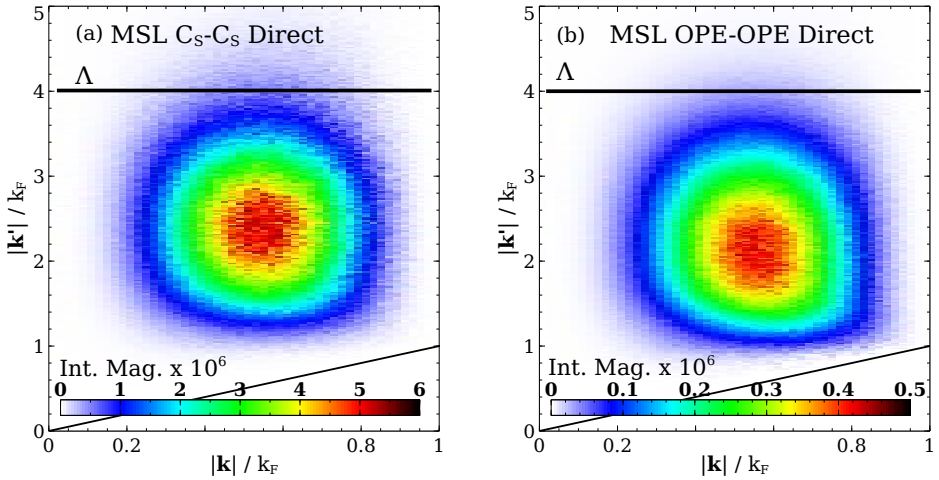

FIG. 20. (color online) Momentum histograms representing the second-order NN phase space for the MSL direct C_S–C_S term (a) and OPE–OPE term (b) at $k_{\rm F} = 0.5$ fm^{-1}, $n = 2$, and $\Lambda_{\rm NN} = 2.0$ fm^{-1}. The exchange and MSNL plots have a similar distribution. The y-axis gives the particle relative momentum while the x-axis gives the hole relative momentum both scaled by $k_{\rm F}$. Colors indicate the $I_{2,\rm full}$ magnitude for a particular k, k' pair. The integrand magnitude $I_{2,\rm full}$ is also scaled by a factor of 10^6. The horizontal black line indicates the cutoff $\Lambda_{\rm NN}$ and the sloping black line separates out the inaccessible region due to Pauli blocking.

These 1-D functions $f(q)$ are plotted in Fig. 27. It can be seen that the functional form of the c_3, c_D terms is monotonically increasing in the momentum transfer q. Taking a large q expansion of the c_3, c_D terms in (E2), where the contribution of the interaction is largest, reveals that c_3, c_D should scale as $q^0 = 1$ or like the scalar term c_E. This exactly matches the ratio behavior as seen in Fig. 26.

In contrast, the c_1 interaction of Fig. 27 reaches a peak near $q \approx 0.7$ fm^{-1}, in the vicinity of the pion mass. This implies that the major contribution to the energy integrals with the c_1 term will come from this region as opposed to the large $|\mathbf{q}|$ area as one would expect for c_3, c_D. As the MSL regulator cuts off in the momentum transfer, we correspondingly expect to see less suppression in the energy values involving the c_1 term.

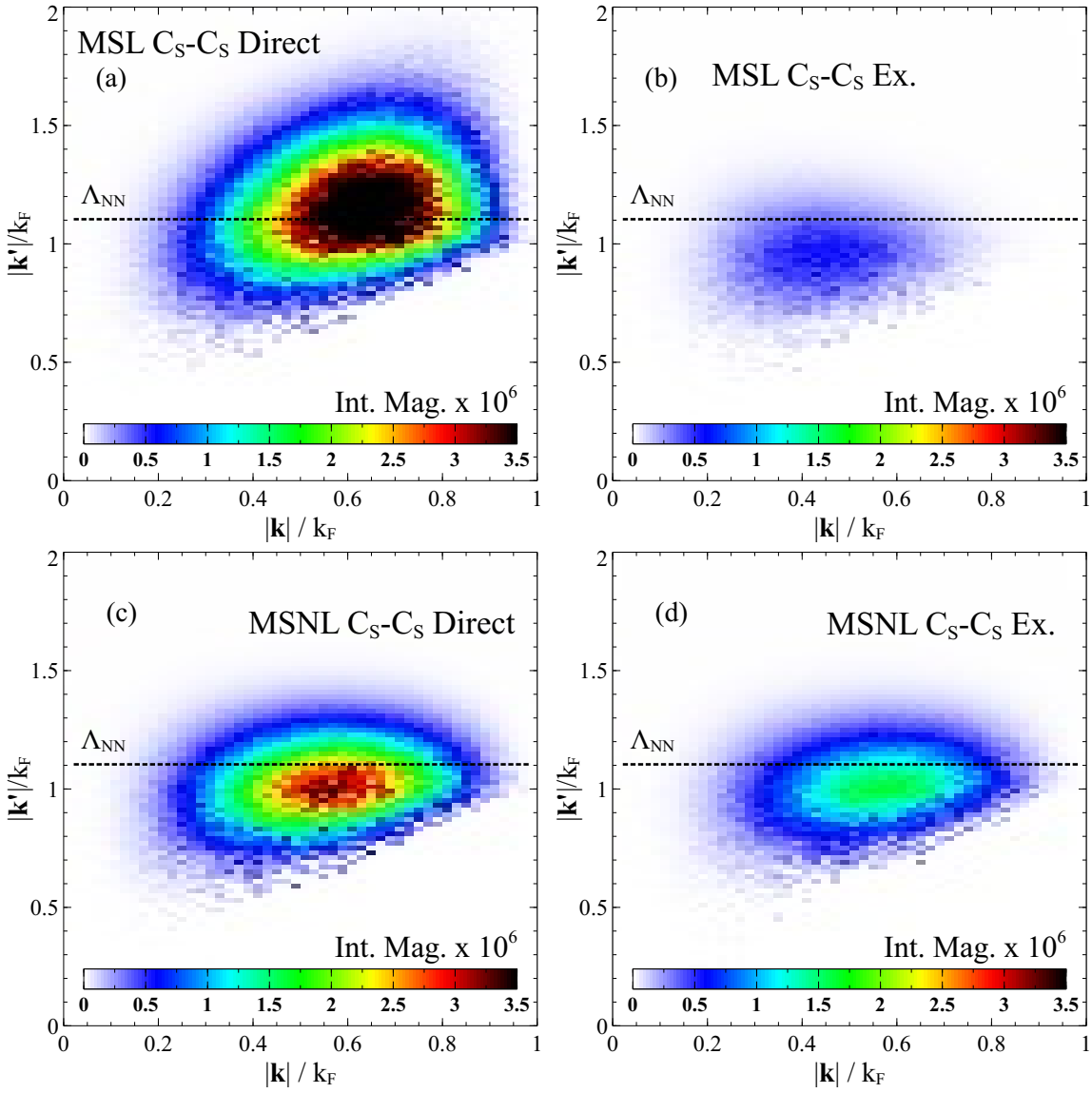

FIG. 21. (color online) Momentum histograms representing the second-order NN phase space for the C_S–C_S term. The MSL direct (a) and exchange (b) terms are shown along with the MSNL direct (c) and exchange (d) terms. Plots done at $k_F = 1.8$ fm^{-1}, $n = 2$, $\Lambda_{NN} = 2.0$ fm^{-1}. The y-axis gives the particle relative momentum k' (35) while the x-axis gives the hole relative momentum k (2) both scaled by k_F. Colors indicate the $I_{2,\text{full}}$ magnitude in (B1) for a particular k, k' pair. The integrand magnitude $I_{2,\text{full}}$ is also scaled by a factor of 10^6.

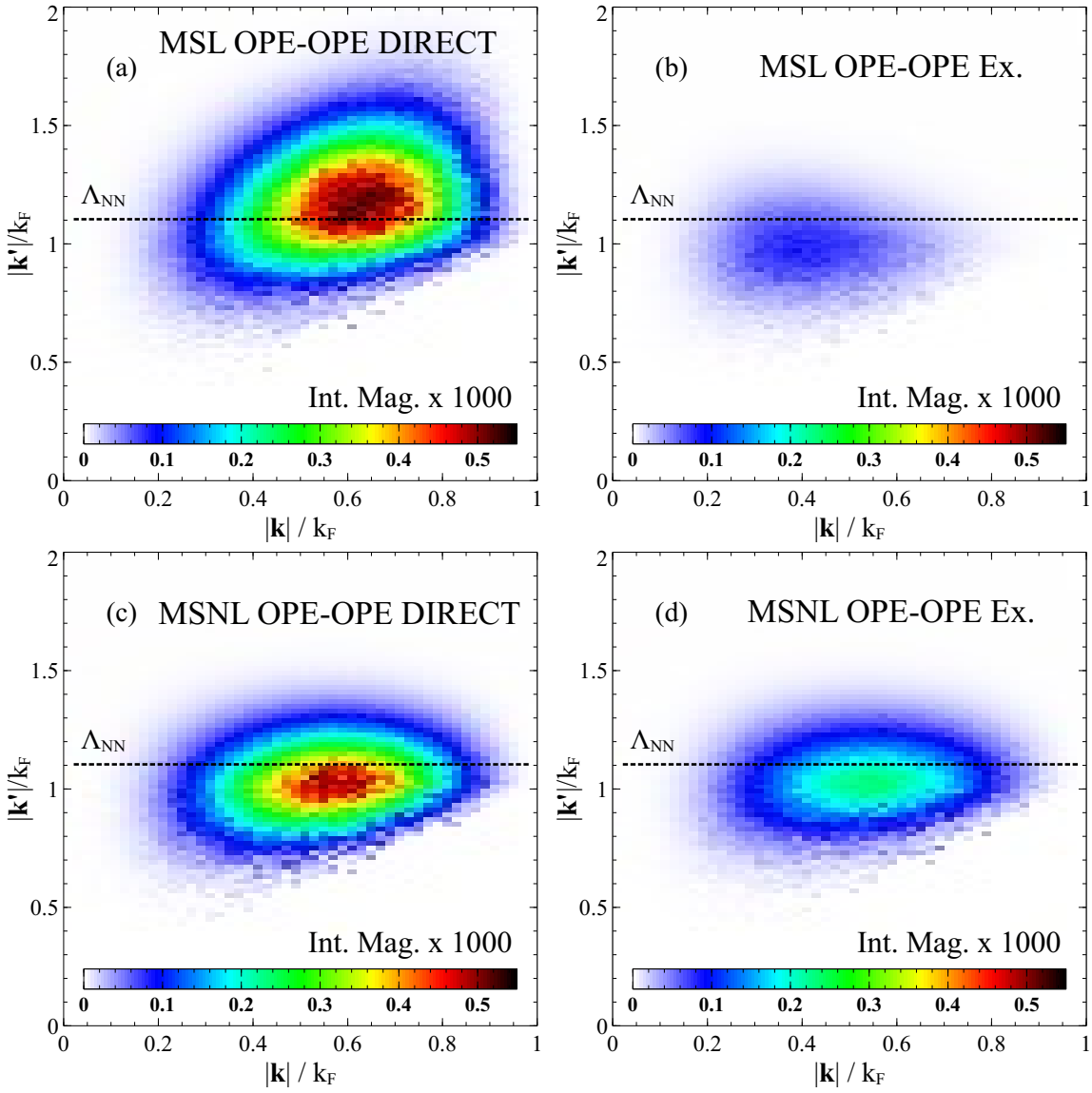

FIG. 22. (color online) Momentum histograms representing the second-order NN phase space for the OPE–OPE term. The MSL direct (a) and exchange (b) terms are shown along with the MSNL direct (c) and exchange (d) terms. Plots done at $k_{\rm F} = 1.8$ fm^{-1}, $n = 2$, $\Lambda_{\rm NN} = 2.0$ fm^{-1}. The y-axis gives the particle relative momentum k' (35) while the x-axis gives the hole relative momentum k (2) both scaled by $k_{\rm F}$. Colors indicate the $I_{2,\rm full}$ magnitude in (B1) for a particular k, k' pair. The integrand magnitude $I_{2,\rm full}$ is also scaled by a factor of 1000.

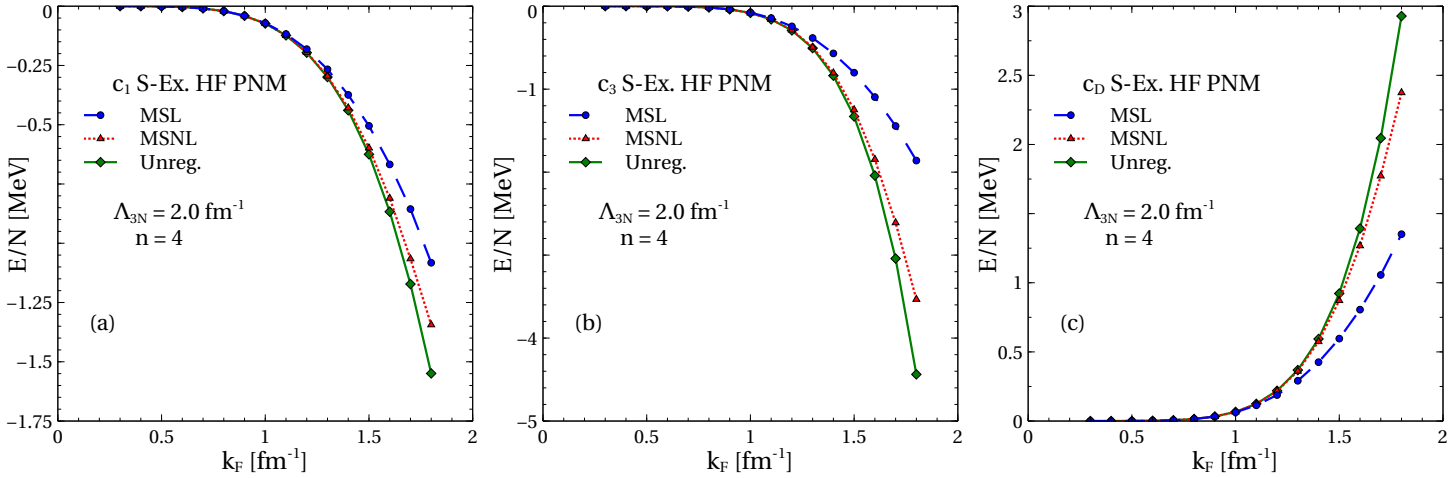

FIG. 23. Plots (a), (b), and (c) show the energy per particle for the single-exchange c_1, c_3, and c_D terms respectively in neutron matter with $n = 4$, $\Lambda_{3N} = 2.0$ fm^{-1}, $c_i = 1$ GeV^{-1}, $c_D = 1$.

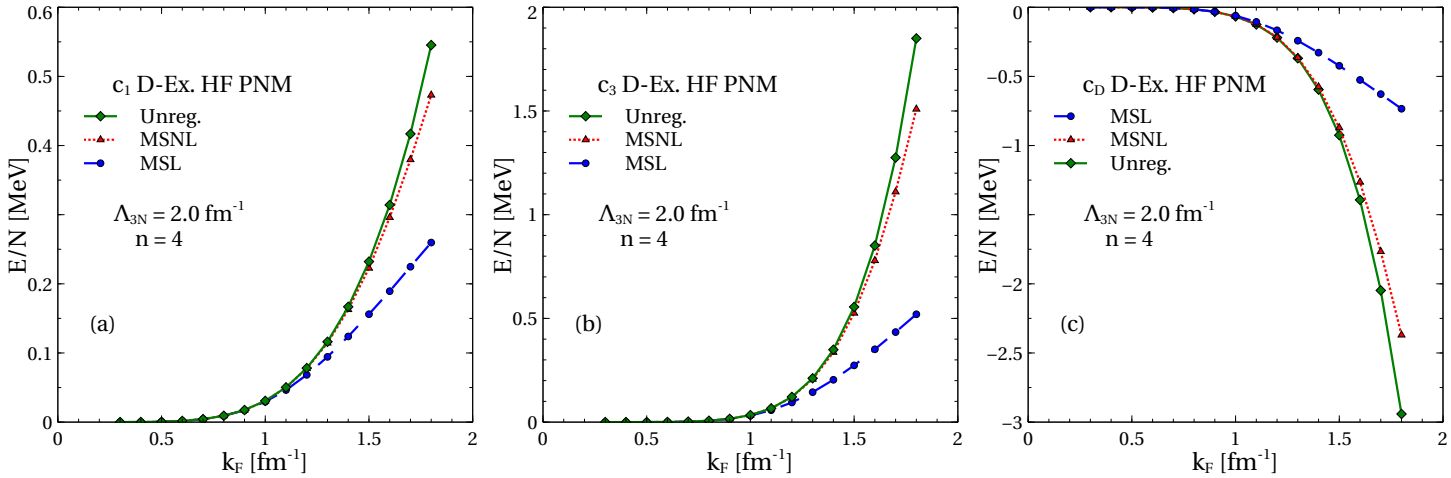

FIG. 24. Plots (a), (b), and (c) show the energy per particle for the double-exchange c_1, c_3, and c_D terms respectively in neutron matter with $n = 4$, $\Lambda_{3N} = 2.0$ fm^{-1}, $c_i = 1$ GeV^{-1}, $c_D = 1$.

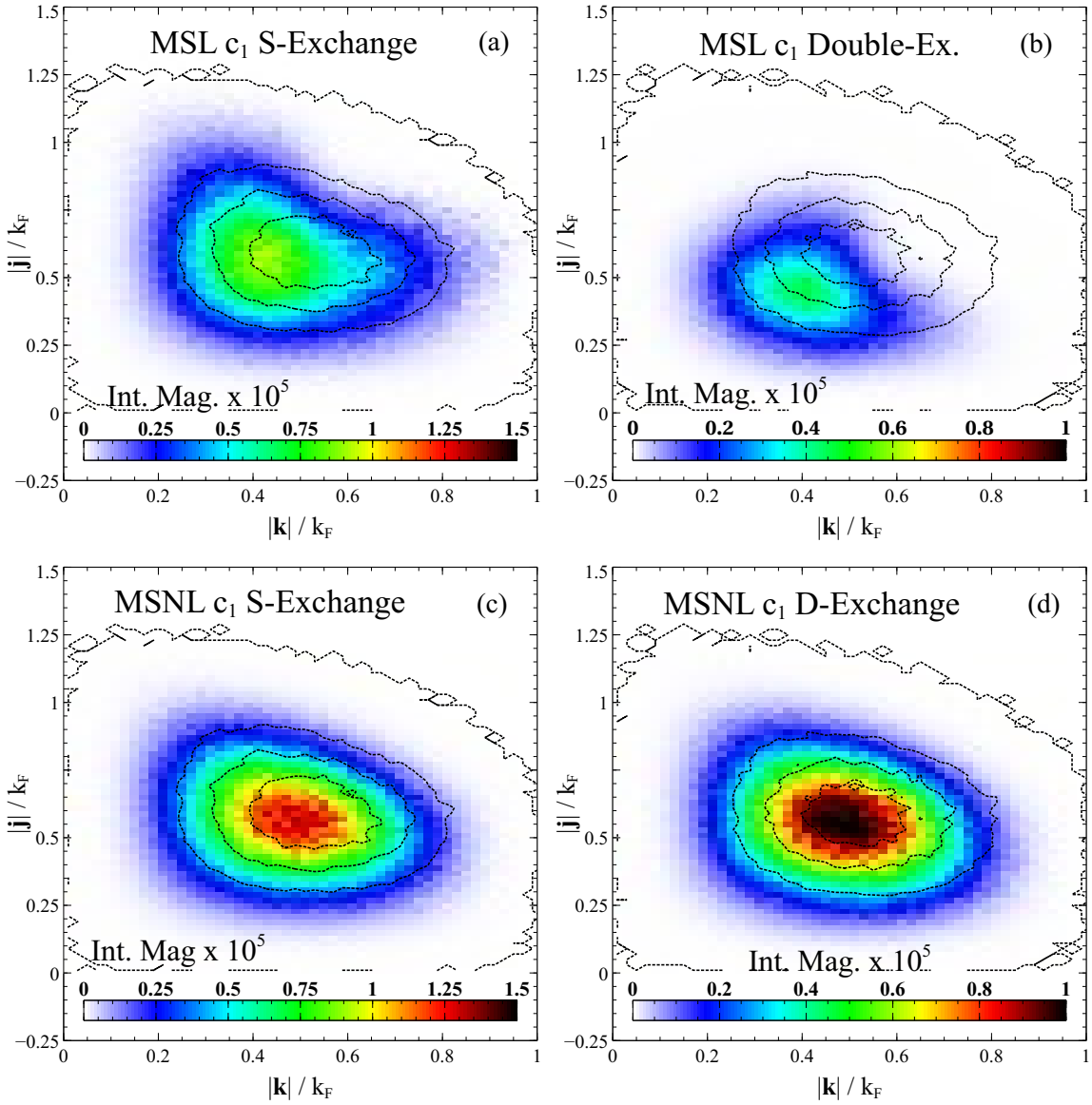

FIG. 25. (color online) Momentum histogram representing the 3N HF phase space for the c_1 term. Plots (a) and (b) show the MSL single-exchange and double-exchange terms respectively. Plots (c) and (d) show the MSNL single-exchange and double-exchange terms respectively. Plotted for $k_F = 1.8, \Lambda_{3N} = 2.0$ fm^{-1}, and $n = 4$. Colors indicate the integrand magnitude I_3 in (39) with a c_1 weight term from (16). The integrand magnitude I_3 is also scaled by a factor of 10^5. Note the change in color scale between the plots.

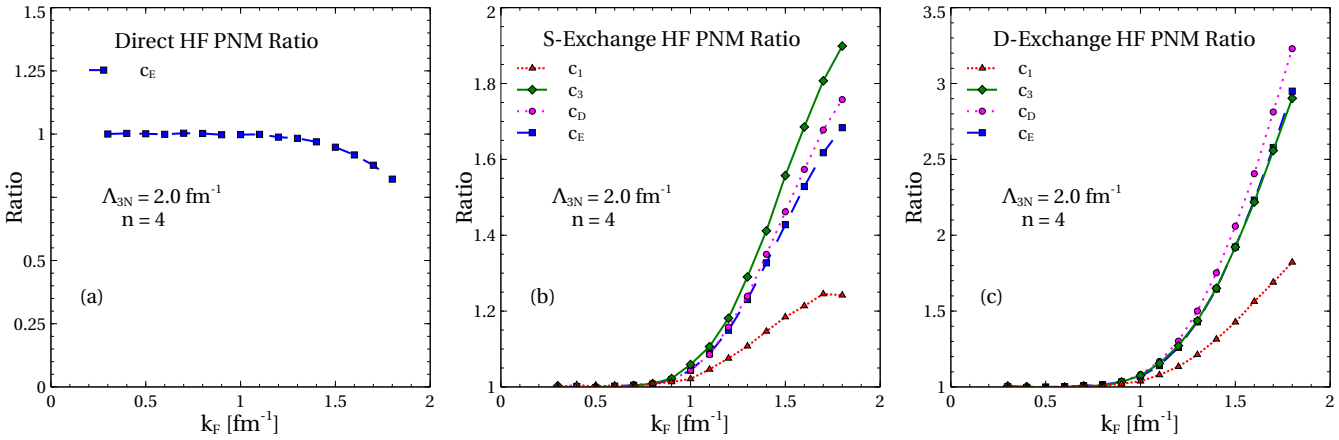

FIG. 26. Ratio of the 3N HF energy, (E1), calculated with the MSNL regulator in (19) to the same energy with the MSL regulator in (22) for the individual 3N interaction terms in PNM. Ratio is plotted for the direct (a), single-exchange (b), and double-exchange (c) terms of the antisymmetric 3N force. The calculations use $c_i = 1.0$ GeV^{-1}, $c_D = 1.0$, $c_E = 1.0$, $\Lambda_{3N} = 2.0\,\mathrm{fm}^{-1}$, and $n = 4$.

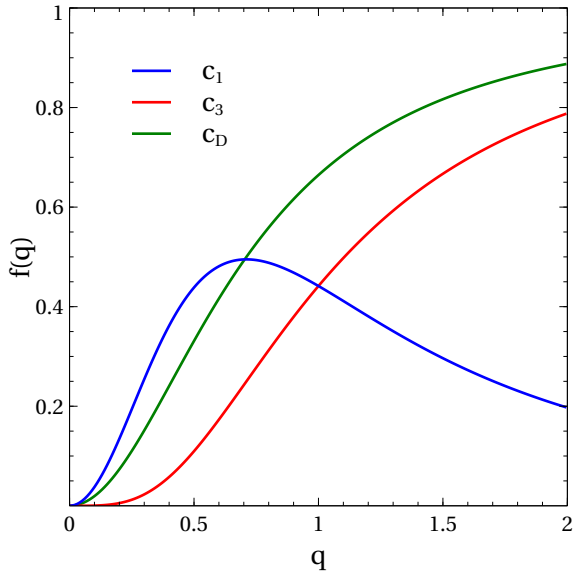

FIG. 27. Plot of the functions $f(q)$ in (E2) which are one-dimensional variants of the finite range 3N interactions ignoring spin-isospin. The functions are plotted as a function of the 1-D momentum transfer q variable.